2024

Development of an X-ray based rigidity analysis method to quantify distraction-osteogenesis fracture healing

BOSTON UNIVERSITY

COLLEGE OF ENGINEERING

Thesis

DEVELOPMENT OF AN X-RAY BASED RIGIDITY ANALYSIS METHOD TO QUANTIFY DISTRACTION-OSTEOGENESIS FRACTURE HEALING

by

SHUBHAM PARASRAJ LAIWALA

B.Tech., Charotar University of Science and Technology, 2022

Submitted in partial fulfillment of the

requirements for the degree of

Master of Science

2024

Approved by

First Reader ____
Ara Nazarian, Dr.Sc..
Associate Professor of Orthopedic Surgery
Harvard Medical School

Second Reader ____
Brian D. Snyder, M.D., Ph.D.
Maurice Edmond Mueller Professor of Orthopedic Surgery
Harvard Medical School

Third Reader ____
Sheila Russo, Ph.D.
Assistant Professor of Mechanical Engineering
Assistant Professor of Materials Science and Engineering

विवेक-धैर्ये सततं रक्षणीये तथाश्रयः |
विवेकस्तु हरिः सर्वं निजेच्छातः करिष्यति

त्रिदुःख सहनं धैर्यमामृतेः सर्वतः सदा |
तक्रवदेहवद्भाव्यं जडवत् गोपभार्यवत्

भक्तद्रोहे भक्त्यभावे भक्तैश्चातिक्रमेकृते |
अशक्ये वा सुशक्ये वा सर्वथा शरणं हरिः

अहङ्कारकृते चैव पोष्य-पोषणरक्षणे |
पोष्यातिक्रमणे चैव तथान्तेवास्यतिक्रमे

अलौकिक मनःसिद्धौ सर्वार्थे शरणं हरिः |
एवं चित्ते सदा भाव्यं वाचा च परिकीर्तयेत्

अविश्वासो न कर्तव्यः सर्वथा बाधकस्तु सः |
ब्रम्हास्त्र-चातकौ भाव्यौ प्राप्तं सेवेत निर्ममः

To my god, parents, mentor, and friends, I couldn’t have done this amazing work without you and your impeccable support. Thank you very much for all the way along.

ACKNOWLEDGMENTS

I would like to thank my guru and my advisor, Ara Nazarian, and my co-advisor Dr. Brian Snyder for their unending patience, their constant support, and their willingness to share skills. Your lab environment has a treasure of knowledge that I am not sure that I will ever find somewhere else.

I could not have done it without my lab mates who I could always bounce ideas off and come away with solutions – Gaberial Lindi, Diana Yeritsyan, Pooja Chainani, Mason Garcia, Ahmad Hedayatzadeh, Nazanin Nafisi, Maria Velasquez Hammerele, Mohammad Khak, Kaveh Momenzadeh, Javad Shariati, and Bella Stewart among everyone else across the Nazarian Lab. I'm honored to have worked with you all. Don't take this work for granted. Thank you, Neel Baxi, Atik Chavda, Devanshi Patel, Abhi Bhalodia, Vraj Shah and Matthew Miceli for always being there.

Thank you, my dearest Mom and Dad, for being my rock in tough times. My mom always taught me to have patience and my dad inspired me to make sure to fight like arjuna from epic tales of Mahabharata. My maternal grandma in my entire journey asked me to have faith in God at every point of my life. To all my friends and family – I truly appreciate you and thank you.

Shubham Amiparasraj Laiwala

Boston University

Mechanical Engineering

DEVELOPMENT OF AN X-RAY BASED RIGIDITY ANALYSIS METHOD TO QUANTIFY DISTRACTION-OSTEOGENESIS FRACTURE HEALING

SHUBHAM PARASRAJ LAIWALA

ABSTRACT

Distraction osteogenesis is used to treat acquired or congenital limb deformities secondary to tumor, infection, or trauma. To lengthen and/or realign a bone, an external fixator is secured to the segment to be transported via trans-osseous pins that stabilize the bone, followed by an osteotomy through which the bone is distracted. While distraction osteogenesis has yielded positive clinical outcomes for a range of skeletal pathologies, the prolonged process of lengthening and waiting 2x that number of days over which the bone was lengthened for the interposed callus to sufficiently ossify to support body weight is taxing. Complications (infection, contractures, neurovascular injuries, pseudo-arthrosis) are correlated with the duration of fixator use. Premature fixator removal results in fracture or recurrent limb deformity. Clinicians make subjective assessments whether the regenerate bone is sufficiently rigid to support weight based on sequential bi-orthogonal radiographs obtained every 4-6 weeks. Guidelines for determining whether fracture callus is strong enough to support body weight are predicated on the presence of at least three continuous cortices, ≥2mm thick, measured on bi-planar radiographs. However, this calculation is subjective, with <50% inter-observer agreement. Using this criterion, reported fracture rates after fixator removal range from 3% to 50%. This variation reflects the inability of 2D bi-planar radiographs to objectively portray the 3D spatial distribution of mineralized callus responsible for its structural stability.

Presented in this thesis is an X-ray based machine learning model inspired from previously developed CT model that predicts on the hypothesis that the structural rigidity of a regenerated bone tissue provides of a *mechanical assay* of the progressive changes in regenerate tissue material properties and anatomical geometry that evolve during distraction osteogenesis and fracture healing. The algorithm accepts biplanar radiographs as inputs, followed by an image processing algorithm to get rid of unwanted noise. Bone Mineral Density (BMD) is predicted from biplanar radiographs, and a Reconstruction Algorithm then predicts 3-Dimensional shape of femur. We have developed an accessible, cost-effective, point of care technology, X-RAY Based Rigidity Analysis Method, which utilizes low-radiation, sequential, biplanar radiographs through fracture callus and regenerate bone to predict its load bearing capacity and failure risk based on calculating the minimal axial, flexural, and torsional rigidities.

In the tranquil embrace of a cozy fall afternoon in 2019, my world was suddenly jolted by the disheartening news of my mother's battle with cancer. The mere utterance of those words shattered the tranquility around me, leaving my heart fragmented into a million pieces. Witnessing her brave journey through treatments, each step laden with both physical and emotional burdens, pierced me to the core.

In the midst of this anguish, a profound determination ignited within me—a resolve born from the depths of love and empathy. It was then, amidst the anguish and uncertainty, that I made a solemn vow to dedicate my life to the pursuit of medical research, particularly in the realm of oncology. My aspiration crystallized: to stand as a beacon of hope for those traversing the arduous path of cancer, to alleviate their suffering, and to contribute tirelessly to the advancement of medical science in the quest for more effective treatments and ultimately, a cure.

Thus, as I embark upon this scholarly journey, it is with profound gratitude and unwavering resolve that I humbly present this thesis. It stands not only as a testament to my academic pursuits but also as a tribute to the countless individuals, like my mother, who confront the formidable adversary of cancer with unyielding courage. May the findings within these pages serve as a testament to the enduring spirit of resilience and hope that defines our collective battle against this insidious disease.

CONTENTS

LIST OF TABLES

LIST OF FIGURES

LIST OF ABBREVIATIONS

AP .... Anterior-Posterior

BMD .... Bone Mineral Density

CT .... Computed Tomography

DEXA .... Dual-Energy Xray Absorptiometry

EA .... Axial Rigidity

EI .... Bending Rigidity

GJ .... Torsional Rigidity

LBC .... Load Bearing Capacity

ROI .... Region of Interest

uCT .... Micro-Computed Tomography

X-ray .... Biplanar Radiograph

Chapter 1

Introduction

1.1 Background

1.1.1 What is Distraction Osteogenesis?

Distraction osteogenesis (figure 1) is an endogenous bone tissue engineering technology that utilizes inherent regenerative capacity to reconstruct or lengthen bone tissues[i]. Initially described in the mandible in Germany in the 1930s, the technique takes advantage of the sequence of events during normal osteogenesis after any bony injury; the initial injury site initially develops a fibrous callus, which subsequently ossifies[ii].

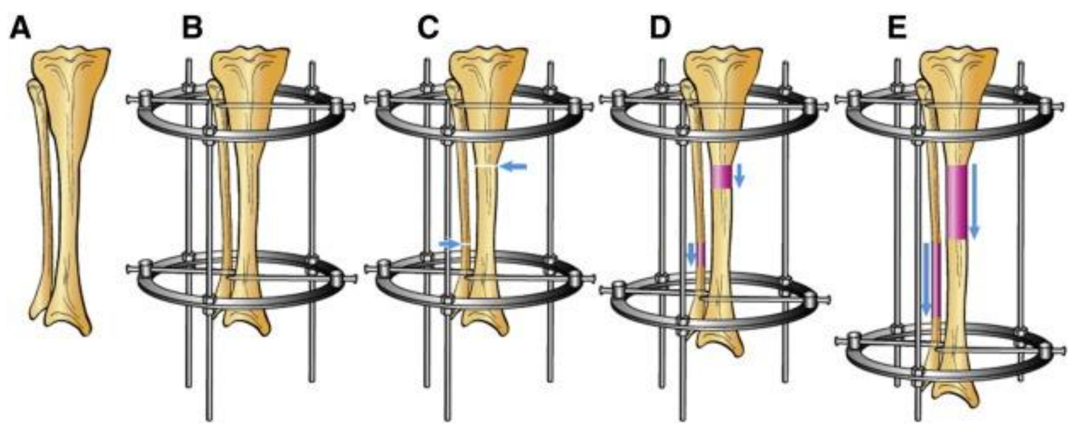

Figure 1: A: Before, B: Fixation of bone, C: Osteotomy, D and E: Distraction

After a short latency period, a distractor is used to distract the bone ends at an appropriate speed and frequency to spontaneously promote new natural bone regeneration in the distraction gap. This period is referred to as the distraction period[iii]. It is used to treat acquired or congenital limb deformities secondary to tumor, infection, or trauma. To lengthen and/or realign a bone, an external fixator is secured to the segment to be transported via trans-osseous pins as shown in figure 2 that stabilize the bone, followed by an osteotomy through which the bone is distracted.

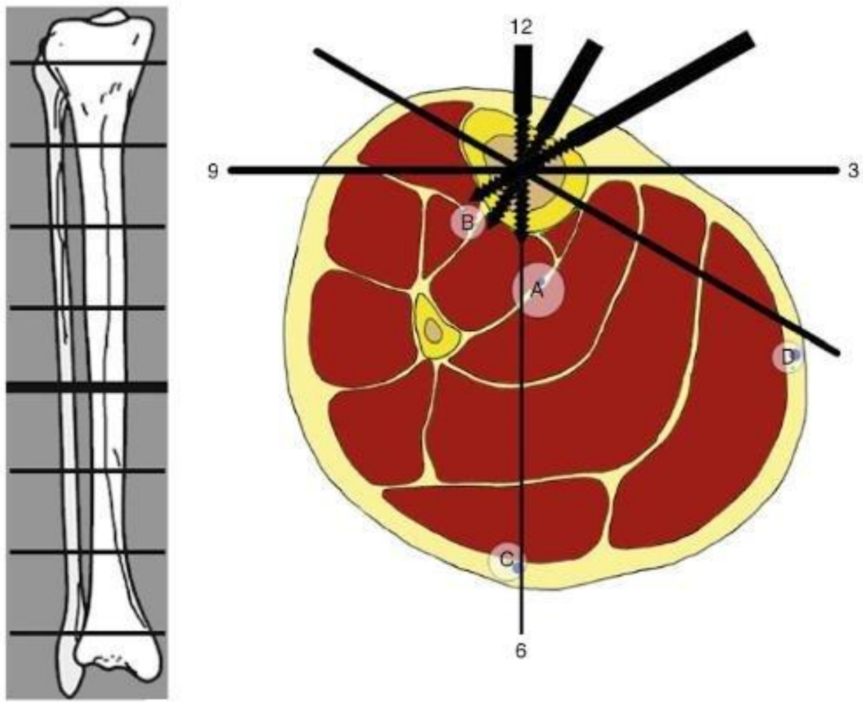

Figure 2: cross sectional view of trans-osseous elements (right)

Distraction Osteogenesis is extremely versatile process and there is no age restriction to perform it, from neonates to adults as long as the patient is physiologically capable to undergo surgery[iv]. It allows for bigger corrections in bone position than is possible in a single traditional surgery. This improves the results and may reduce the amount of surgery an individual needs over their lifetime. In both distraction osteogenesis and traditional Bone Grafting procedures, surgeons make a cut in a bone. There may be similarities between these two procedures, but the underlying difference is in traditional surgery the doctor uses bone grafts to lengthen bones. In some cases, a bone is moved and held in its new position with metal plates and screws. Whereas, in Distraction Osteogenesis a surgeon attaches a device called a distractor as shown in figure 3 to the cut bone. If the fracture is not immobilized, this ossification will not complete and a fibrous union result. While this is undesirable after an accidental fracture (the basis for casting or other rigid fixation after fractures), the intentional movement of an osteotomy along a controlled vector gradually stretches this fibrous callus, which is subsequently immobilized allowing ossification. The net result is a lengthening of the bone at the site of the osteotomy.

Figure 3: Distractor used in Distraction Osteogenesis

This technique has become widely used for malformations of the cranial skeleton and is used to elongate the mandible, midface, and calvarium. The advantages of the approach are its creation of strong bone in a controlled manner, resistance to relapse, and adaptive changes of the soft tissue envelope[v]. While the new bone is being formed it undergoes three stages of fracture healing: inflammation, repair, and remodeling. During Inflammation Stage a hematoma forms at the fracture site and growth factors are secreted by hematopoietic cells in the hematoma. Fibroblasts migrate to the fracture site in response to transforming growth factor-beta (TGF-Beta) and other cytokines and granulation tissue forms at the fracture site. Fibroblasts and osteoblasts then proliferate at the fracture site. In the Repair Stage, Formation of the primary soft callus begins (Figure 4). Ossification occurs as fibroblasts differentiate into chondrocytes expressing type 2 collagen, which are gradually replaced with type 1 collagen (woven bone). This process is dependent upon many cytokines, particularly tumor necrosis factor-alpha (TNF-Alpha). This is the stage utilized by distraction osteogenesis. The initial soft callus is allowed to form, and then a mechanical force is applied to stretch the callus without breaking it, resulting in lengthening. In third and final stage of Remodeling, Chondrocytes present undergo terminal differentiation involving numerous signaling pathways, some involving parathyroid hormone-related peptide (PTHrP) and bone morphogenetic protein (BMP). The extracellular matrix becomes calcified, and type X collagen is expressed as chondrocytes undergo apoptosis. New blood vessel ingrowth is stimulated by vascular endothelial growth factor (VEGF), and the resultant woven bone enters organized osteoblast/osteoclast remodeling [vi].

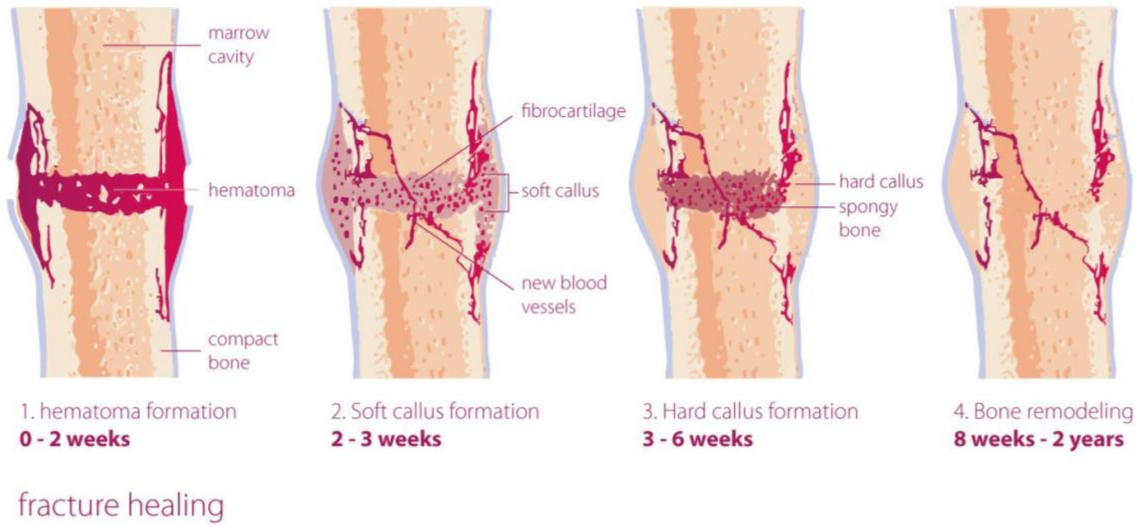

Figure 4: Fracture Healing and Bone Remodeling

In Distraction Osteogenesis, the distractor occasionally is placed under the skin. Whereas most of the times it is attached to an individual's bones on the outside of their skin. The type of distractor used depends on the bones that need to grow. The devices are approved by the Food and Drug Administration. All devices are made of a lightweight hypoallergenic metal called titanium.

1.1.2 Problems associated with Distraction Osteogenesis

While distraction osteogenesis has yielded positive clinical outcomes for a range of skeletal pathologies, the prolonged process of lengthening the bone 1 mm/day and waiting at least 2x that number for the interposed callus to ossify sufficiently to support body weight is taxing. Complications such as infection, contractures, neurovascular injuries, pseudo-arthrosis, Relapse, Device Failure, Device Extrusion, Tooth bud Injury, Scarring or Cerebrospinal Fluid Leak are correlated with the duration of fixator use.

Relapse: In Distraction Osteogenesis, some degree of Relapse is bound to happen. In craniofacial distraction, Relapse and long-term results have been reported in several clinical studies and resulted in adjustment of the distraction protocol to include over correction of 15–25%.[viiviiiix]

Device Failure: In the review by Swennen et al., the most common complications were device-related problems, IAN neurosensory disturbances, and infection[x]. These types of failure are advanced technical complications, necessitating general anesthesia for correction. According to Raoul et al., Van et al. and Von et al. 10% of treated patients encountered Device Failure problems which required replacement[xixiixiii] . According to Ow et al. and Van et al. 9% of treated individuals have reported breaking of Distraction rod [xiv] [xv]

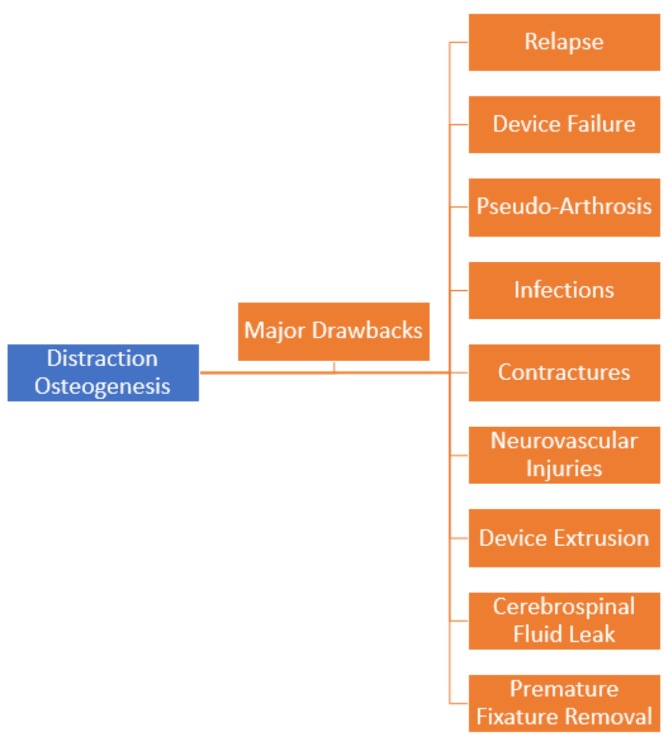

Besides above-mentioned complications correlated with the duration of fixator use, a major impediment to successful treatment of limb deformity by distraction osteogenesis is the high incidence of fracture and recurrent deformity following fixator removal (**Table 1**). Clinicians make subjective assessments regarding the ability of healing bone to support load based on bi-planar radiographs and clinical criteria that have been demonstrated to be inaccurate for predicting the bone's load bearing capacity [xvi]. In a classic study from the BIDMC lab, Hipp et al. demonstrated that experienced orthopedic surgeons, including the pioneering orthopedic oncologist, Henry Mankin, MD could not accurately estimate strength reductions or the load bearing capacity of bones with simulated defects using bi-planar radiographs or CT[xvii].

Table 1: Fracture rates in patients treated by distraction osteogenesis.

Study	Number	Rates	Bone Treated
Simpson (2000) [xviii]	17/180	9.4%	Femur & Tibia
Launay (2012) [xix]	20/111	18.0%	Femur & Tibia
Kitoh (2014) [xx]	17/70	24.0%	Femur & Tibia
Burke (2017) [xxi]	8/176	4.5%	All femur
Eldridge (1991) [xxii]	17/571	3.0%	No Noted
Danziger (1995) [xxiii]	9/18	50.0%	All Femur
Castelein (2016) [xxiv]	10/51	20.0%	Femur & Tibia

1.1.3 Development of Rigidity Analysis Method to Quantify Distraction Osteogenesis Based Fracture Healing

The Beam is one of the fundamental structural members. A beam, sometimes is referred to as a flexural member, can be thought of as a structure that spans the distance between supports and is loaded primarily in a transverse direction. Rigidity is the structural property that incorporates both the material and geometric properties of fracture callus that dictate its load bearing capacity. We propose to improve the safety and efficacy of distraction osteogenesis by using rigidity as a mechanical assay to accurately predict the load bearing capacity of fracture callus. We are developing an accessible, point of care technology, X-ray-based Rigidity Analysis solution, which utilizes low-radiation, Bi-planar X-ray images through healing and pathologic bone[xxv] to predict its load bearing capacity and failure risk based on calculating the minimal axial, bending, and torsional rigidities. Clinicians make subjective assessments regarding the ability of healing bone to support load based on bi-planar radiographs and clinical criteria that have been demonstrated to be inaccurate for predicting the bone's load bearing capacity[xxvi]. In a classic study from the BIDMC lab, Hipp et al.[xxvii] demonstrated that experienced orthopedic surgeons, including the pioneering orthopedic oncologist, Henry Mankin, MD could not accurately estimate strength reductions or the load bearing capacity of bones with simulated defects using bi-planar radiographs or CT.

Although bone mass is highly correlated with bone strength, nearly 30% of the variation in bone strength is attributed to other factors such as the composition of the non-mineralized, organic matrix and the structural organization of the tissue at macro- and microscopic scales. Ultrasound (US) uses acoustic energy to assess bone material properties by measuring the attenuation of a sound wave as it passes through the tissue. Sound wave transmission is modified by the structure, composition and mass of the tissue, all of which contribute to its mechanical competence. The velocity of a sound wave transmitted through a tissue varies as the ($\sqrt{}$(tissue modulus)÷(tissue density)). Since US is accessible, portable, inexpensive, and does not expose patients to ionizing radiation, it has been used to evaluate fracture callus formation and endochondral ossification during fracture healing and distraction osteogenesis. US has been shown to detect osteogenesis at the distraction site up to 3 weeks earlier than standard radiography or DXA [xxviii] [xxix] [xxx]. However, due to the inability of US to penetrate the outer cortex of mature bone, US is limited in its ability to monitor changes in bone stiffness and strength beyond a certain level of fracture healing. Using a rabbit model of distraction osteogenesis of the tibia, proposed by Luk et al., broadband linear B-mode US was compared to computerized digital radiography to monitor endochondral ossification of the distracted fracture callus. Speed of sound transmission and acoustic reflection through the fracture callus during early distraction predicted osteogenesis (i.e., bone mineral density and microstructural properties measured by micro-computed tomography, μCT) of the regenerate bone at the end of treatment (adjusted R^2 = 0.43–0.67). However, the rather low R^2 values, and the predictive capability of the modality at early healing phases, articulates the need for a better approach.

1.2 Innovation

Bi-orthogonal digital radiography is the most common modality used to assess whether the regenerate bone in the distracted segment is sufficiently rigid to support body weight. It offers advantages of decreased radiation exposure, accessibility, and low cost. An X-ray examination is the most traditional and standard monitoring method. It is a technique that is used to measures bone tissue mineral content and is commonly used to diagnose osteoporosis. In this work we propose to develop a technology which predicts on the hypothesis that the structural rigidity of a regenerated bone tissue provides of a *mechanical assay* of the progressive changes in regenerate tissue material properties and anatomical geometry that evolve during distraction osteogenesis and fracture healing. We aim to improve the safety and efficacy of distraction osteogenesis and other treatment approaches such as the Papineau bone grafting technique for limb salvage by using the X-Ray Based Rigidity Analysis Method. Given that we are harnessing this technology in a new but related application, this work will be immediately translatable to the treatment of patients and provide impetus for a prospective clinical study to demonstrate the safety and efficacy of X-Ray Based Rigidity Analysis Method to predict the load bearing capacity of distracted fracture callus.

Chapter 2

Image Segmentation

2.1 Development of new method for Image Segmentation

Segmenting unwanted regions from the image has been a fundamental problem in computer vision since early days of the field [xxxi]. Image Segmenting for development of X-ray based Rigidity Analysis machine learning model to quantify Distraction Osteogenesis Fracture Healing, involves partitioning of an input X-ray image into cortical component and trabecular components. Moreover, Image Partitioning plays a vital role in varieties of applications in visual understanding of systems of machine vision, object detection, medical imagining, and video surveillance to name a few. In simple words, Image segmentation can be named as an issue of classifying pixels with semantic labels, or partitioning objects, or both [xxxii]. Various image segmentation techniques have been developed in literature from most basics such as Thresholding[xxxiii], K-means clustering[xxxiv], Histogram-based thresholding (Otsu Method) to advanced algorithms such as graph cuts[xxxv], active contours[xxxvi] and Sparsity based methods. In recent years machine learning models with similar models have been developed. Most of these models have numerous human inputs which compromised their accuracy and computational speed. However, in this work have developed a machine learning tool which can automatically calculate the thresholding intensity and use it to convert the input Xray dicom to the binarized image. The binary image is then segmented into cortical and trabecular segments based on their grayscale indices.

In variety of applications involving visual inspection, it is required to separate objects from background of an image taken under condition of poor and non-uniform illumination. Given that the target objects may appear to be lighter or darker than background, thresholding is one of the techniques to isolate the target objects from background. Image thresholding is a simple, yet effective, way of partitioning an image into a foreground and background. This image analysis technique is a type of image segmentation that isolates objects by converting grayscale images into binary images. A certain threshold level between 0 to 1 is automatically selected by algorithm developed by Ridler et al. [xxxvii].

A common method of automatically deriving at which to segment a given X-ray picture is to examine its gray level histogram[xxxviii]. The grayscale histogram is initially segmented into two parts using a starting threshold value such as 0 = 2B-1, half the maximum dynamic range.

Now, to automatically calculate thresholding intensity, Ridler et al. proposed to compute global threshold of the grayscale image using Iterative Threshold Selection. During this stage the exact locations of the osseous matter and its background are unknown. In its first approximation background and osseous materials are differentiated using Iterative Threshold Selection method and it is used as a switching function f(s) to route digitalized image into one of two integrators as indicated into by a schematic diagram figure 5.

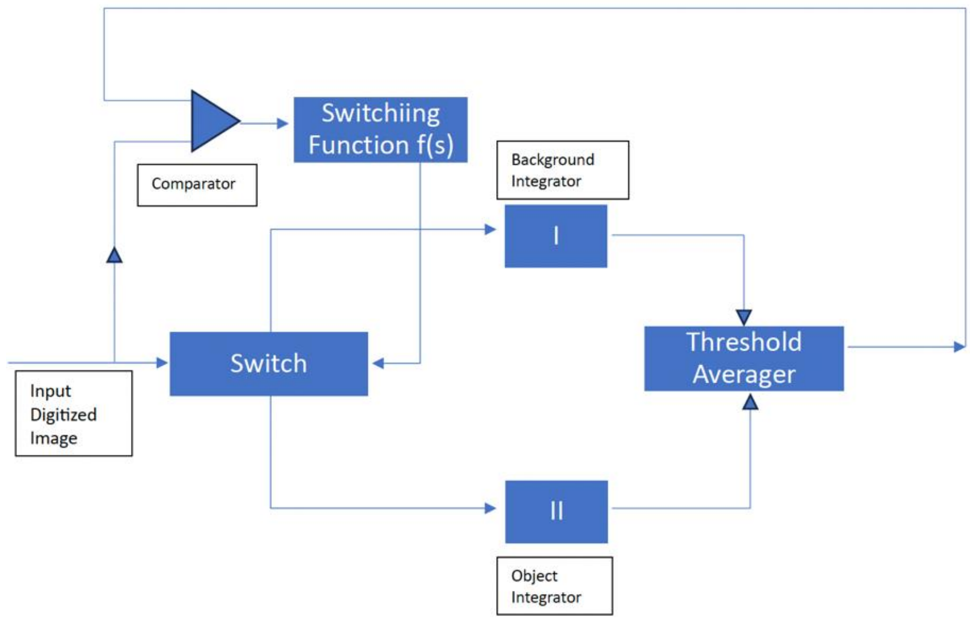

Figure 5: Schematic Image Processing Diagram for Iterative Image Thresholding

The thresholding intensity calculated by the code developed by Ridler et al. is used to convert Xray Dicom to binary image. Apart from extracting cortex, the binarized image comprises of various unwanted segments of tissues.

According to this method, if f(s) = 0 then input Xray Dicom is directed towards Integrator I and is considered as a background. However, if f(s) =1 then input Xray Dicom is directed towards Integrator II and is considered as an osseous material. This process is repeated for each pixel of grayscale image. Lastly, automatic calculated threshold intensity from Ridler et al. is incorporated into our developed machine learning model which labels '1' to every image pixel whose gray level is *above* (f(s) = 1) than threshold intensity and '0' to every image pixel whose gray level is *lower* (f(s) = 0) than threshold intensity. The distinct brightness regions in a grayscale image are indicated by presence of peaks in histogram. It is therefore considered reasonable to choose a threshold intensity midway between the peaks. The calculated threshold will then differentiate between clearly between the modes of histogram. The binarized version generated using

Iterative Selection Method of input X-ray dicom are illustrated in figure 6.

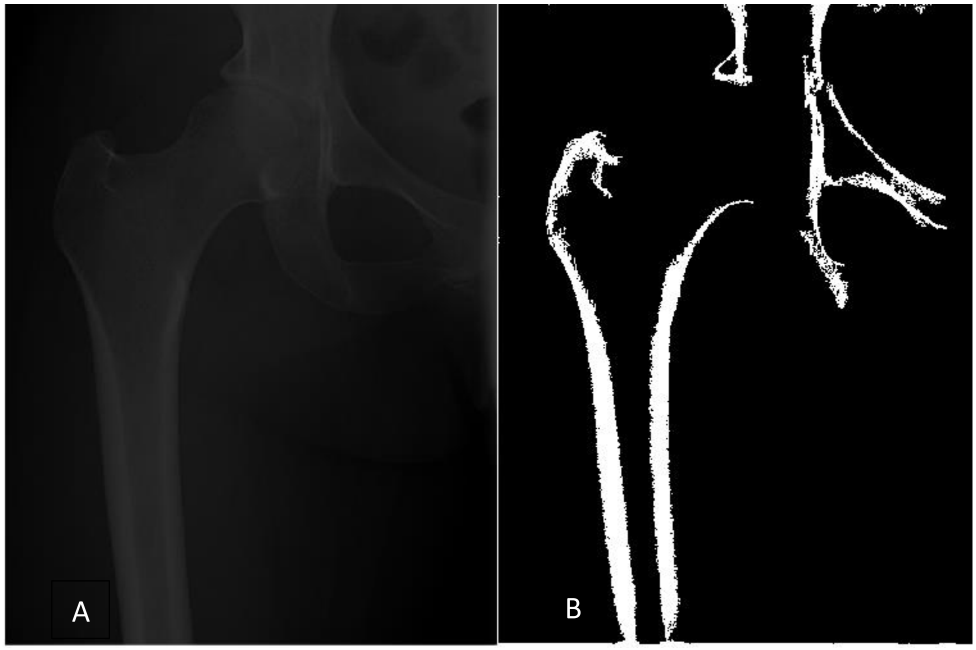

Figure 6.1: (a) the left side of figure shows input Xray Dicom, (b) right side of figure shows automatically thresholded image.

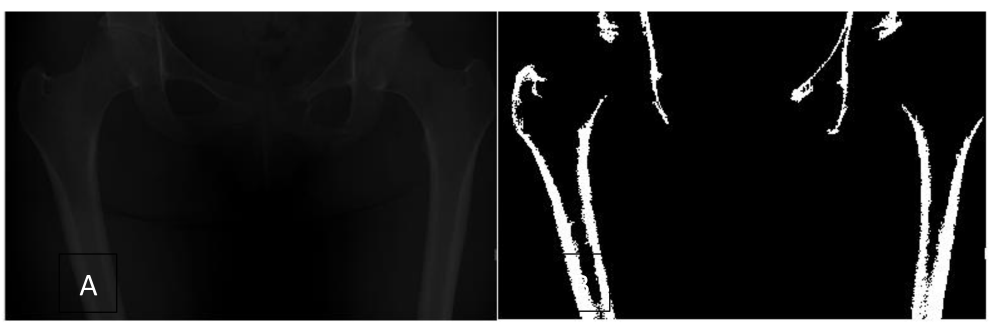

Figure 6.2: (a) the left side of figure shows input Xray Dicom, (b) right side of figure shows automatically thresholded image.

According to Linda et al. [xxxix] and Barghout et al. [xl] final goal of image segmentation is to simplify and/or to change representation of image into something that is much simpler and easier to understand. In simpler words, Image Segmentation is a process to assign label to every pixel in an image and pixels with similar labels have identical characteristics. However, there are numerous pixels which were assigned similar labels during conversion of Xray Dicom to binary image which do not have similar characteristics to their original nature. In this case subcutaneous fat and some regions of muscles are labelled as cortex. This unwanted label can be termed as noise. Digital images are prone to various types of noise.

Noise is the result of errors in the image acquisition process that result in pixel values that do not reflect the true intensities of the real scene. There are several ways that noise can be filtered out of an image, depending on how the image is created. In this work we have trained a model which computes the pixel weights, where the reference grayscale intensity value is the average of the intensity values of all the pixels in image that are marked as logical true in mask. Using the average of several pixels to calculate the reference grayscale intensity value can be more effective than using a single reference intensity value. Finally, the image is filtered using Pillbox filter and it is later masked over original Xray Dicom to have a clear idea of exact location of cortical composition of a femur. The results of this trained model are depicted in figure 7:

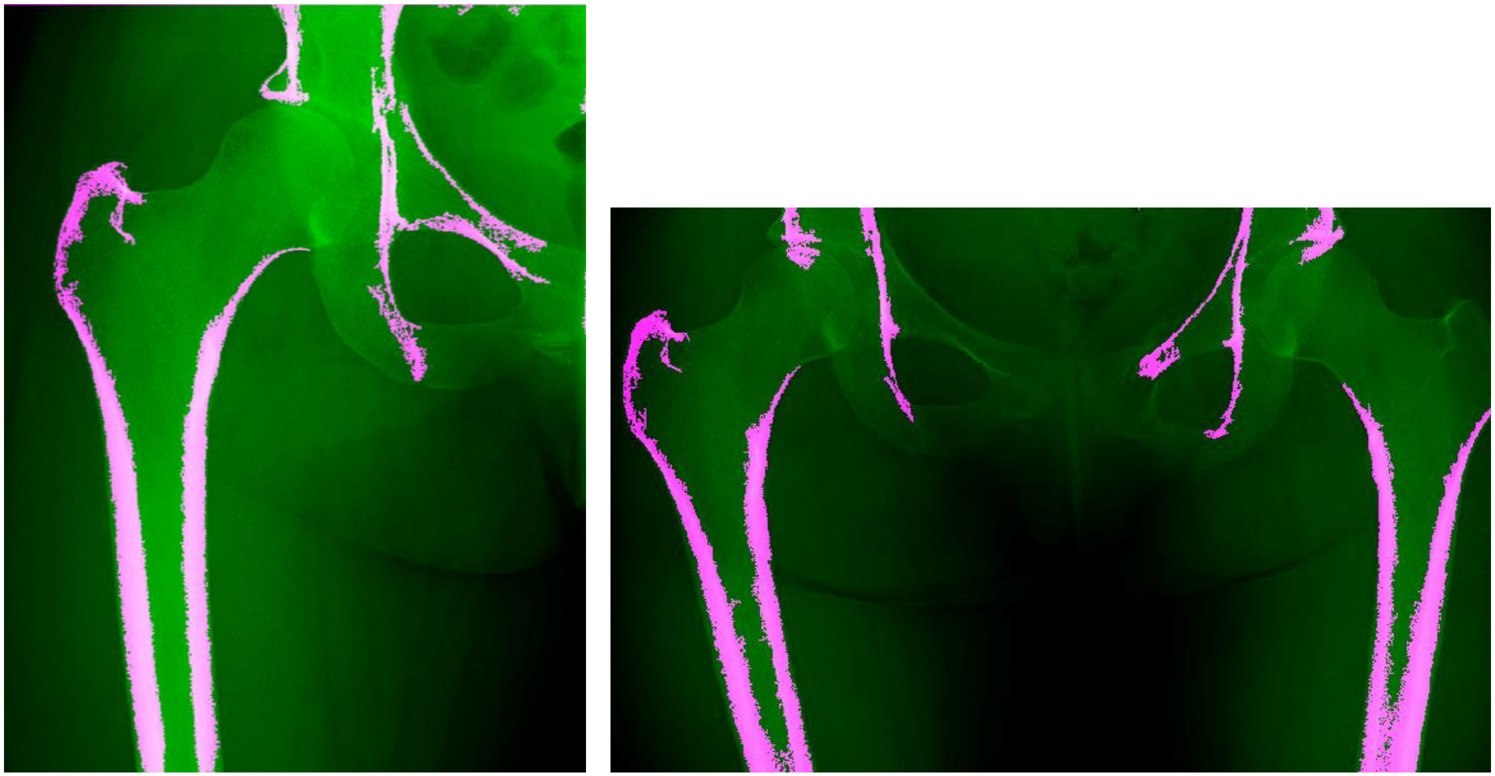

Figure 7: final extracted cortex masked over the original X-ray Dicom

Chapter 3

Bone Mineral Density

3.1 What is Bone Mineral Density

Numerous complications like infection [xli] [xlii], stiff joints[xliii] and early union are the associated with limb lengthening. Fractures have been reported several times after fixator removal. According to Launay et al. 3–50% of reported fractures are associated with limb lengthening[xliv]. Moreover, there was no fixed pattern and location of fractures reported. Simpson et al. conducted a study on 173 patients undergoing distraction osteogenesis. In this study 17 fractures were reported; six were within the regenerate itself, six at the junction between the regenerate and the original bone and five at distant sites in the limb. Despite of the principles of distractions are applied and the callotasis technique has been very popular since last 7 decades or more, the rates of fracture occurring after distraction osteogenesis remains significant high. These principles are essential to obtain optimal union of the distraction site, and to limit the risk of fracture after removal of the external fixator.

Clinicians employ several non-invasive procedures may be used to evaluate bone union and determine when the external fixator should be removed, such as ultrasound, Dual Energy X-ray Absorptiometry (DEXA) osteodensitometry which provides quantitative and qualitative evaluation of bone, as well as digital X-ray and CT scan [xlv] [xlvi] [xlvii] [xlviii] [xlix] [l] [li]. However, in most centers, the most common technique is standard anteroposterior X-ray as shown in figure 8, because it is simple to use, inexpensive and accessible. X-rays travel in a straight line with beams diverging from a source. The initial structures hit by a beam will be magnified in relation to those closest to the detector. Therefore, structures that need to be measured with better accuracy need to be placed closer to the detector. The central ray is a simplified way of indicating the direction in which an x-ray beam travels. Different projections describe how the central ray travels through anatomy. Anterior-posterior denotes that the central ray passes first through the anterior anatomy and exits posteriorly, while the posterior-anterior denotes that the central beam passes from posterior to anterior. These terms also give an indication of which structures are closer to the detector.

Figure 8: AP and Lateral view of femur

During the lengthening process in Distraction Osteogenesis new bone tissue is being formed. The rigidity of the new bone tissue depends upon the amount of calcium and phosphorous deposited as hydroxyapatite during bone mineralization process. The composition of these minerals' accounts for 70% of bone composition; remaining 30% is mostly organic matter, mostly collagen. The development process of a bone in fracture healing phase is extremely complex process of interrelated events in space and time leading to formation of new bone. There are two major processes involved in bone formation: Intramembrous bone formation and Endochondral bone formation. Both of these processes involve transformation of a preexisting mesenchymal tissue into bone tissue [lii]. The direct conversion of mesenchymal tissue into bone is called intramembranous ossification. This process occurs primarily in the bones of the skull. In other cases, the mesenchymal cells differentiate into cartilage, and this cartilage is later replaced by bone. The process by which a cartilage intermediate is formed and replaced by bone cells is called endochondral ossification.

The overall mechanical strength of cortical and cancellous components of bone depends upon bone geometry, density, and mineral properties[liii]. The strength of a bone is determined by its structure and material properties; Bone Mineral Density (BMD) is a very useful tool for diagnosis of above-mentioned bone properties. The quantity of mineral content in a bone is provided by its BMD. It is a biophysical parameter of critical experimental importance. Higher BMD is the indication of more mineral concentration which leads to a denser bone as indicated in Figure 8. While the new bone is being formed during distraction phase, the mineral content of the bones being formed will be lower leading to lower BMD. As the newly forming bone is weak and brittle, it escalates the risk of fracture. Fracture risk markedly increases when bone mineral density is less than 1 g/cm^2. Hence, it is extremely important to come with a method which measures the mineral density of bone with minimal exposure to radiation.

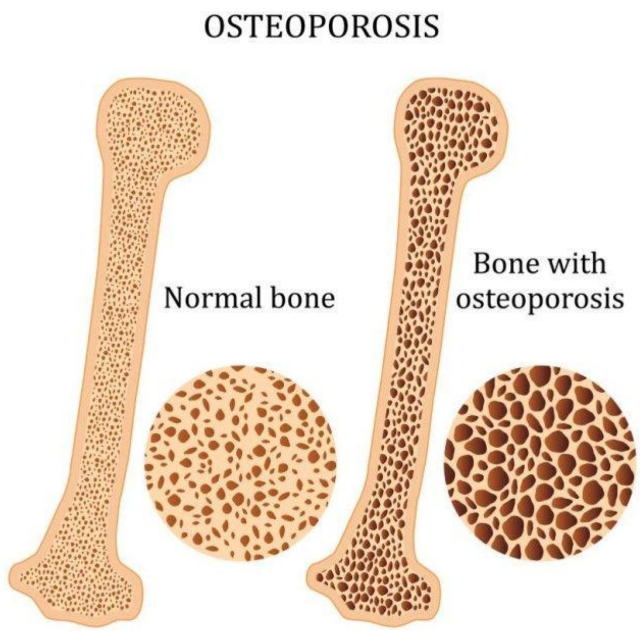

Figure 9: Normal bone vs. osteoporotic bone

3.2. Techniques to Measure Bone Mineral Density (uCT, Dexa and Pycnometry)

The accurate measurement of bone mineral density using noninvasive methods can be of value in the detection and evaluation of primary and secondary causes of decreased bone mass. Multiple methods have been developed for quantitative measurement of bone mineral mass. These procedures have progressed from the use of radioactive sources such as gadolinium-153 to more rapid x-ray techniques, including CT. Advances also include moving from single- to dual-energy techniques[liv].

3.2.1. Dual-Energy Techniques

Dual-energy techniques are especially important for areas such as the spine and hips, where soft tissues can have considerable impact. By comparing a lower energy beam or photon that is attenuated by bone and soft tissue with a higher energy source that is affected only by bone (or metal), it is possible to calculate the differential absorption, allowing more accurate assessment of bone density without impact from the surrounding soft tissues [lv].

1. Dual-Energy X-Ray Absorptiometry

   The past decade has observed a rapid evolution of new radiological techniques to quantify the skeletal composition and integrity [lvi]. More than any other method introduction to Dual-Energy X-Ray Absorptiometry (DEXA) [lvii] [lviii] [lix] has been responsible for the recent rapid growth in the clinical applications of the bone densitometry.

   The DEXA beam comprises of photons or X-ray of 2 distinct energies, precluding the need of assumptions about soft tissue shape and attenuation. This method also allows for evaluation of thicker body parts and bones involving complex geometry, such as the femoral neck and the spine. The fundamental physical principle behind DEXA is the measurement of the transmission through body of x-ray with high and low photon energies. Because of the dependence of the x-ray attenuation coefficient on atomic number and photon energy, measurement of the transmission factors at two different energies enables the areal densities (i.e., mass per unit projected area) of two different types of tissue to be inferred. In DEXA scans these are taken to be bone mineral (hydroxyapatite) and soft tissue respectively [lx]. The basic working principles of DEXA can be explained by following equations:

Low Energy:

$$I' = I'_0\, exp - (\mu'_s M_s + \mu'_b M_b) \qquad (1a)$$

High Energy:

$$\mathrm{I} = I_0 \exp - (\mu_s M_s + \mu_b M_b) \qquad (1b)$$

Where μ is the mass attenuation coefficient, M is the areal density and subscript b & s denote bone and soft tissue respectively.

<u>Accuracy and Precision:</u> The accuracy of a method to measure physical quantity reflect the degree to which measured results deviate from the original values. It is a standard practice of defatting and ashing the bone in a muffle furnace to get true Bone Mineral Content (BMC). Despite the obvious importance of validating the bone densitometry there are only few studies which have reported the accuracy of DEXA [lxi]. Comparison of in vivo BMD measurements of cadavers with the results of post ashing portrayed the difference of 0–15%.

3.2.2. Computed Tomography Techniques:

3.2.2.1. Introduction:

MicroCT is an X-ray imagining method to visualize bone at microstructural scale for 3-dimensional assessment of bone morphology of small animals. MicroCT is considered as a gold standard. As applied to the small bones, it can effectively assess parameters such as density estimation, porosity, structure thickness, and morphometric analysis [lxii].

When X-ray is focused on an object, it's intensity is attenuated based on the material parameters (Fig. 10). An X-ray detector opposite to the object measures the changes in X-ray energies and creates the projection of subjected object. Clinical CT (and in vivo MicroCT) works by acquiring multiple projections as the source and detector rotate around the object (e.g., patient, mouse), and reconstructing these projections into a 2D tomogram or CT slice[lxiii]. Because, the density of bone mineral is relatively higher than its surroundings, it attenuates X-ray energy much more than its surrounding and thus a clear contrast is provided between bone and adjacent nonmineralized tissue by MicroCT scans (Fig. 11). For bone MicroCT, standard practice is that the linear attenuation is converted to mineral density based on a hydroxyapatite (HA) calibration phantom, as bone mineral is like hydroxyapatite. Thus, the units of bone mineral density (BMD) from MicroCT are [mg HA/cm3]. In summary, MicroCT attenuation values may be expressed per mille or as BMD [mg HA/cm3].

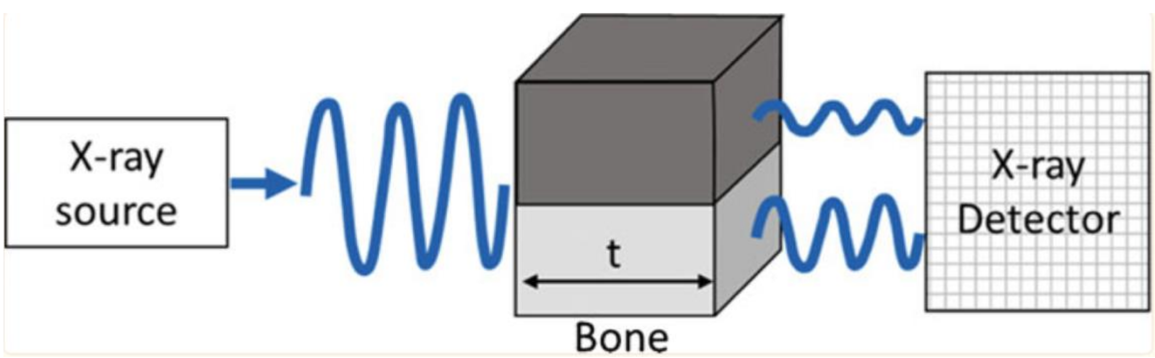

Figure 10: Mechanism of X-ray imagining

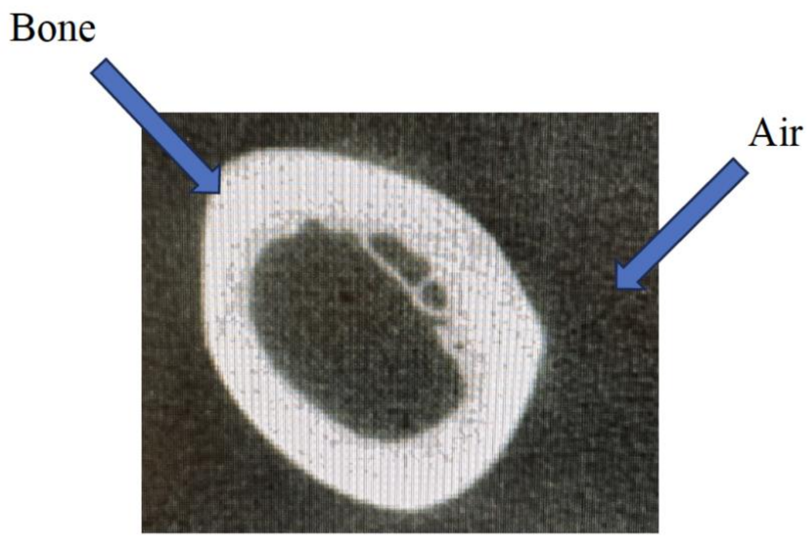

Figure 11: MicroCT scan of rat femur

3.2.2.2 Materials and Methods

1. **Animal Selection and euthanasia:**

   Mention mice and rats to most people and images of unsanitary conditions and urban decay come to mind. Rats have been vilified as the carriers of the infected fleas that led to the dreaded Black Plague that decimated Europe, North Africa, and Central Asia in the fourteenth century. It has been suggested recently that an apology is in order and that other influences, not rodents, were to blame[lxiv]. However, Animal models, and more specifically rodent models, have been extensively used and have contributed greatly to the development and establishment of a wide range of approaches to regenerate the bone tissue. For instance, and focusing on osteogenesis, rodent models have provided great amount of data regarding the cellular behavior of multiple populations relevant to bone regeneration [lxv] [lxvi] [lxvii].

For this experiment rodents were our primary choice of animals because they continue to model their skeleton throughout their life cycle – regarding growth and reshaping – and growth plates remain open throughout adulthood. Compared to large animal models, they are inexpensive, easy to manipulate and easy to house. Moreover, due to their widespread utilization, much is known regarding the biological processes associated with bone turnover, diet modifications and drug administration. Furthermore, the reduced lifespan of these animals allows for the study of the influence of ageing in the bone metabolism and regeneration processes.

The optimal choice of euthanasia method for laboratory rodents depends on several factors, including the scientific goals of the study, the need to minimize animal pain and/or distress, applicable guidelines and laws, the training and proficiency of personnel, and the safety and emotional needs of the personnel performing the euthanasia. Following the methods suggested by Shomer et. al CO_2 euthanizing method was chosen. At the time of euthanizing rats were 15 weeks old. The animal is placed inside the container and a cartridge is activated, thereby sending carbon dioxide into the chamber. A flow limiting orifice and noise muffler are incorporated into the system preventing distress in the animals.

After the rats are euthanized a 2 mm incision was made near urethral orifice towards lateral flank of thigh. The abdominal skin was pulled to expose abdominal cavity without impairing the integrity of peritoneal cavity. To expose dorsum pedis the skin of anterior surface was dissected downwards of hind limbs. The skin the posterior surface was preserved for better fixation as shown in Fig. 12.

Figure 12: Isolation of Femur and Tibia, ankle joint was transected as shown in arrow.

The patella and articular surface of knee joint was exposed after removing tibia (figure 13A). The femoral capitulum was isolated by tightly holding articular capsule with a pair of scissors and rotating it towards the versed genuflex of a knee joint (figure 13B). The surrounding soft tissue were further cut with scissors towards proximal end to reveal three quarters of the length of a femur (figure 13C and figure 13D). Remaining muscles attached to the head of femur were then simply pulled with a cotton gauze to obtain a clean femur (figure 13E).

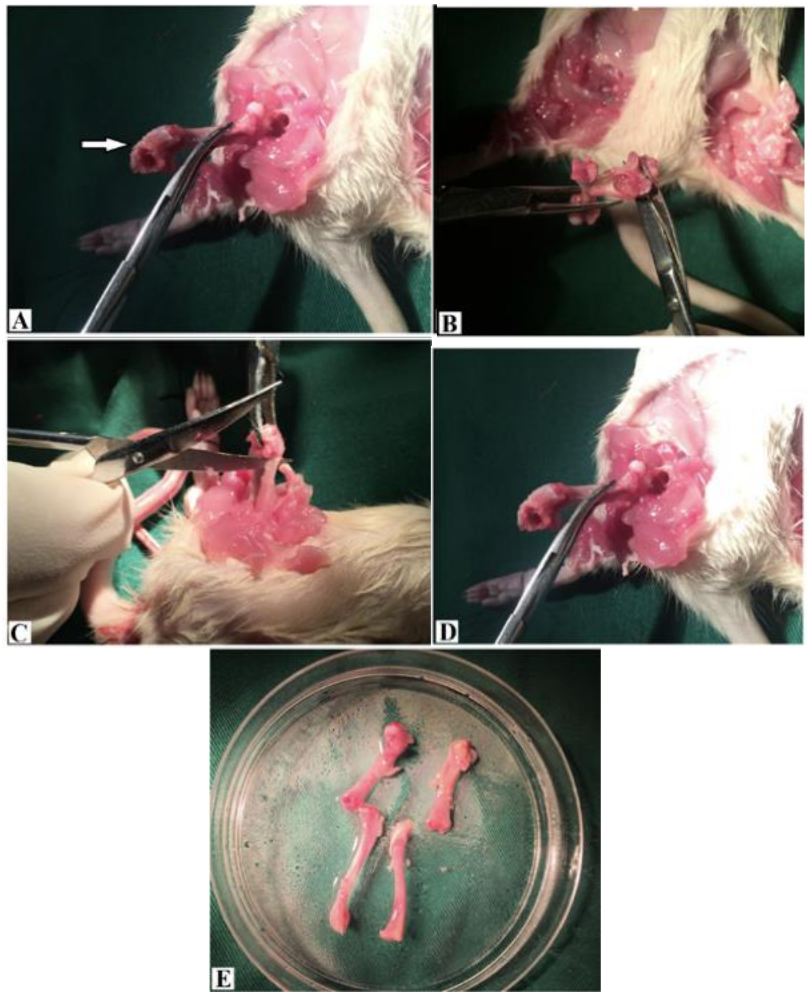

Figure 13. A: Patella is indicated by an arrow, B: Femur Capitulum isolated, C: Sheer force applied by scissor to isolate femur, D: removing remaining muscle tissue, E: clean femur and tibiae obtained.

2. **Materials required to measure BMD.**
   2.1 Scano μCT 40 (Scano Medical, Switzerland).
   2.2 Sample holder (Scano Medical).
   2.3 Phosphate buffered saline.
   2.4 Parafilm

3. Methods to measure BMD using MicroCT:

The methods below were followed for the MicroCT scanning and analysis for intact mouse femur, using a specimen scanner.

After the rodents were euthanized, the femurs were removed from them. The specimen was secured to with the parafilm and then it was placed in the sample holder. During the scanning period, the specimen must remain hydrated. For this purpose, specimen was submerged in phosphate buffered saline solution which was poured in the sample holder (figure 14(bone in sample holder)). The sample holder is than placed in scanner. The *start position* and *end position* of the Scout view is adjusted. Reference lines are determined by the users before scanning begins.

Once the scans are generated, bones are contoured. For contouring, region of interest around the bone is delineated by using automatic methods. Data are evaluated after segmentation which involves applying filters to the image data. Finally, in 3D evaluation window, a script which calculates Bone Mineral Density is selected which then evaluated the mineral density of the bone subjected to scans.

An overview of these steps is shown in figure 14

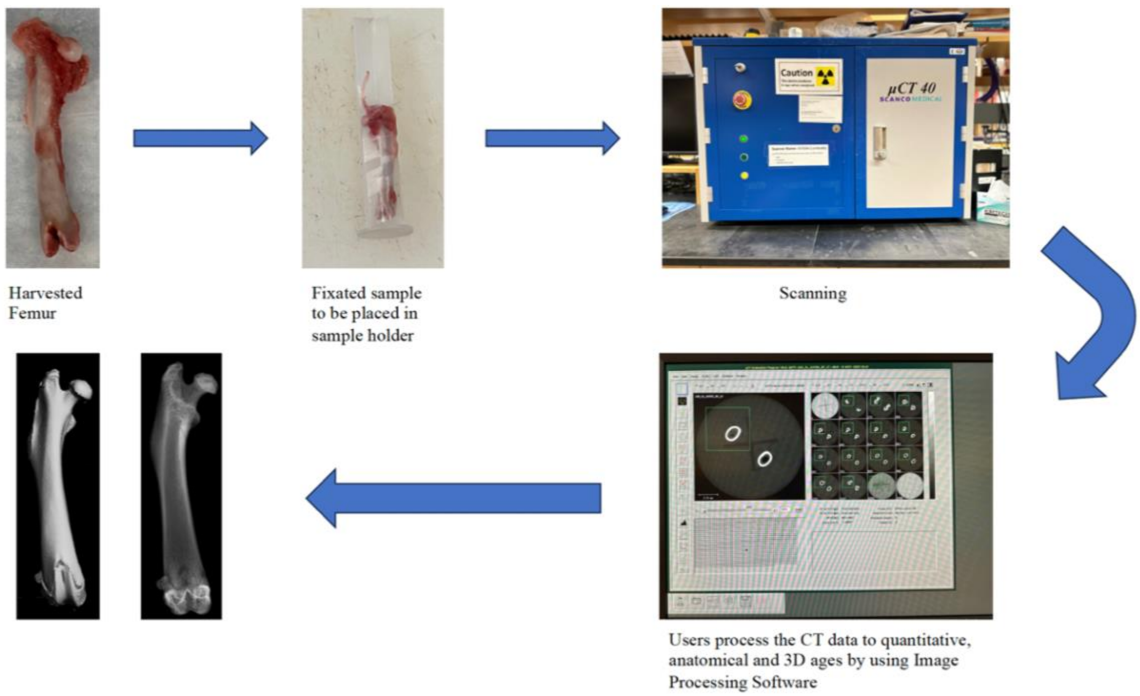

Figure 14: workflow of MicroCT scanning

Chapter 4

Necessity for Development of an X-Ray Based Rigidity Analysis Method

4.1 Drawback of Computed Tomography:

Although there are numerous advantages of using Computed Tomography from rapidly acquiring images to provide clear and specific information, drawbacks like radiation toxicity, contrast-induced nephropathy and the escalating cost of computed tomography scans cannot be ignored. In a survey of 4 major hospitals in Houston it was found that the charge for CT of head, chest or abdomen including contrast but excluding the radiologist fee ranges from 1400$ to 2500$. Not only the cost but also the concerns regarding radiation have always been rising along with the tendency to use CT is inappropriate. Table 2 indicates effective dose from different examinations in diagnostic radiology [lxviii].

Table 2: Effective dose from different examinations in diagnostic radiology.

Examination	Average Effective Dose (mSV)	Examination	Average Effective Dose (mSV)
Chest X-ray (PA)	0.02	CT chest	7
Chest X-ray (PA and Lat)	0.1	CT chest for pulmonary embolism	15
Abdomen	0.7	CT abdomen	8
Pelvis	0.6	CT pelvis	6
Skull	0.1	CT three phase of liver	15
Lumbar Spine	1.5	CT skull	2
Mammography	0.4	CT neck	3
IVP	3	Coronary CT angiography	16
Upper GI Study	6	Virtual Colonoscopy	10

While CT scanning provides a great benefit in medicine, but it also becomes a major source of X-ray exposure. Radiation doses from CT scans are much higher than conventional radiographs and it raises the concerns about carcinogenic potentials. Another major concern using CT scan is the main concern of using CT imaging is the risk associated with ionizing radiation. Ionizing radiation can either damage DNA directly or cause the formation of hydroxyl free radicals capable of mutating DNA, or damaging cells. In turn, this can lead to skin injury and increased risk for cancer, as seen in various studies presenting a dose-dependent risk of cancer development in patients who are exposed to radiation. CT scans generally expose patients to an effective radiation dose of 1-10 millisieverts (mSv), presenting a real risk for patients. Thus, reducing the CT scan dose to the equivalent of a plain chest X-ray would significantly minimize the risk for developing cancer without sacrificing its accuracy as a diagnostic tool. As a result of this concerns, we propose a method which uses bi-orthogonal digital radiography is the most common modality used to assess whether the regenerate bone in the distracted segment is sufficiently rigid to support body weight.

Within the pipeline of the developed software, axial (EA), bending (EI) and torsional rigidities (GJ) for each transaxial cross-section image are calculated by summing the modulus-weighted area of each voxel comprising the bone section by its position relative to the centroid of the bone. Axial rigidity provides a measure of the bone's resistance to deformation when subjected to uniaxial loads. Bending rigidity provides a measure of the bone's resistance to bending deformation when subjected to bending moments. Torsional rigidity provides a measure of the bone's resistance to twisting deformation when subjected to torsional moments.

The moment of inertia (I) is a tensor; therefore, its magnitude depends on the orientation of the bone cross-section relative to the direction of the applied bending moment. To account for this, we solve the eigenvalue problem and determine the principal values I_{max} and I_{min}. Assuming a worst-case scenario, we use the minimum principal value, I_{min}, when tabulating the bending rigidities for each sequential cross-section through the bone.

4.2 Innovation: Calculating Bone Mineral Density using Bi-planar radiographs.

To calculate bone mineral density from biplanar radiographs the radiation energy per pixel or a picture element i.e. the amount of bone in each pixel is converted into an 'areal density'' which is measured in g/cm^2. The number of pixels in area is summoned. This method allows a bone density to be calculated for the specific bone in question.

4.2.1 Isolating femur from background noise

The developed algorithm reads biplanar radiograph of a rat femur and it is converted to a grayscale image. After the radiograph is converted to a grayscale image, a 'region of interest' which is also known as a 'relevant measurement range' is created to reduce computational load on the algorithm and to elevate the algorithm's efficiency & speed. A rectangular region of interest as shown in figure 16 was developed for working with the radiographs of rat femur. Once the ROI is created and well defined the gaussian filter is applied to reduce noise.

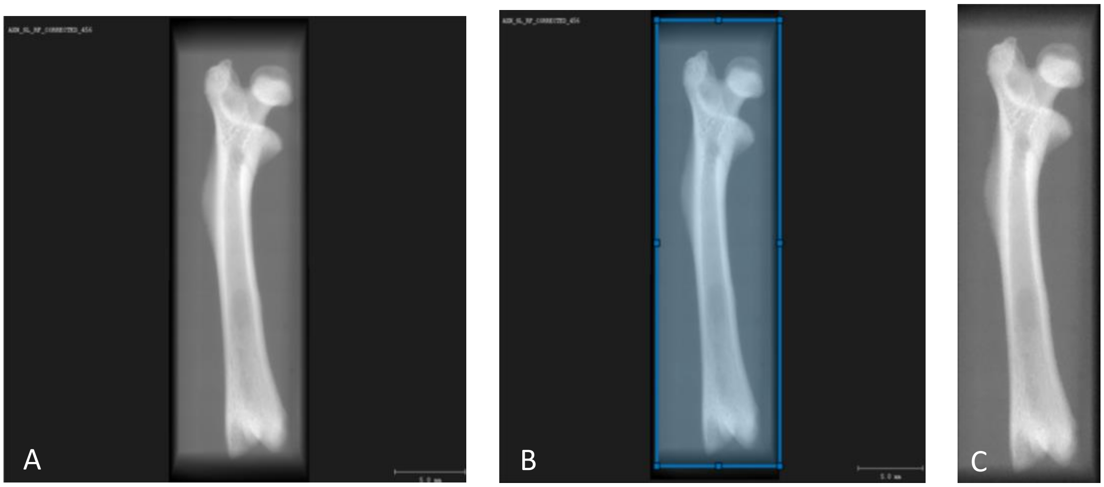

Figure 15, A: The original X-ray dicom from uCT, B: ROI is developed to reduce computational time, C: post ROI image processing.

In an uncorrupted image, the values of neighboring pixels are expected to be correlated (because an object or surface generally spans multiple neighboring pixels). Noise in neighboring pixels, on the other hand, is often uncorrelated. reducing the noise in an image is thus by "averaging" neighboring pixels. Such methods are often referred to as "filtering." Commonly used filters include mean filter (a.k.a. uniform filter), which replaces the value of a pixel by the mean value of an area centered at the pixel; Gaussian filter, which is like a mean filter but weighted in favor of pixels closer to the center.

After the noise reduction using gaussian filter, the target object (rat femur) is surrounded by unwanted whiteness which could be termed as a lens flare as shown in the figure 16A. It could lead to numerous computational and calculation errors if it is left untreated. To isolate the target object from surrounding noises a global thresholding

Figure 16A: Lens fare surrounding femur

method was developed. In this method the pixels of a given picture are represented in L gray levels [1, 2, ..., *L]*. The number of pixels at level *i* is denoted by n_i and total number of pixels by $N = n_1 + n_2 + \cdots + n_i$. The probability distribution can be given by [lxix] [lxx] [lxxi]

$$P_i = \frac{n_i}{N}, P_i \geq 0, \sum_{i=1}^{L} P_i = 1 \tag{3}$$

Now, in this method the pixels are classified into 2 classes C_o(background object) and C_1(target object) by a threshold at a level *t,* C_o denotes pixels with gray levels [1, 2, …, *t*] and C_1 denotes objects with gray levels [*t+1, …, L*], then the probability of class occurrence and class mean are

$$\omega_0 = P_r(C_o) = \sum_{i=1}^{t} P_i = \omega(t) \tag{4}$$

$$\omega_1 = P_r(C_1) = \sum_{i=t+1}^{L} P_i = -\omega(t) \tag{5}$$

And

$$\mu_0 = \sum_{i=1}^{t} i\, P_r\left({}^{i}/_{C_0}\right) = \sum_{i=1}^{t} i\, \frac{P_i}{\omega_0} = \frac{\mu(t)}{\omega(t)} \tag{6}$$

$$\mu_1 = \sum_{i=t+1}^{L} i\, P_r\left(\frac{i}{C_1}\right) = \sum_{i=t+1}^{L} \frac{P_r}{\omega_1} = \frac{\mu_T - \mu(t)}{1 - \omega(t)} \tag{7}$$

Where ω_t and μ_t are 0th and 1st order cumulative moments of the histogram up to t^{th} level and are defined as follow

$$\omega(t) = \sum_{i=1}^{t} P_i \tag{8}$$

$$\mu(t) = \sum_{i=1}^{t} iP_i \tag{9}$$

And μ_t is the total mean level of the original image which is computed as

$$\mu_T = \mu(L) = \sum_{i=1}^{t} iP_i \tag{10}$$

Once the threshold level is calculated of a grayscale image, it is then converted into a binary image to mask out the unnecessary white noise as shown in figure 17B. Binary images are imaging whose pixels have only two possible intensity values. Numerically, the two values are often 0 for black, and either 1 or 255 for white. The main reason binary images are particularly useful in the field of Image Processing is because they allow easy separation of an object from the background. The process of segmentation allows to label each pixel as ‘background’ or ‘object’ and assigns corresponding black and white colors. The 0’s are assigned to the background pixels and 1’s are assigned to target object as shown in figure 16B. Finally, to separate the bone from the surrounding noise, the binary mask matrix is multiplied with the original grayscale which renders the final image which just consists of useful bone structure figure 17.

Figure 16B: Binary mask

Figure 17: Final image without lens flare

The entire flowchart of image processing is show on figure 18:

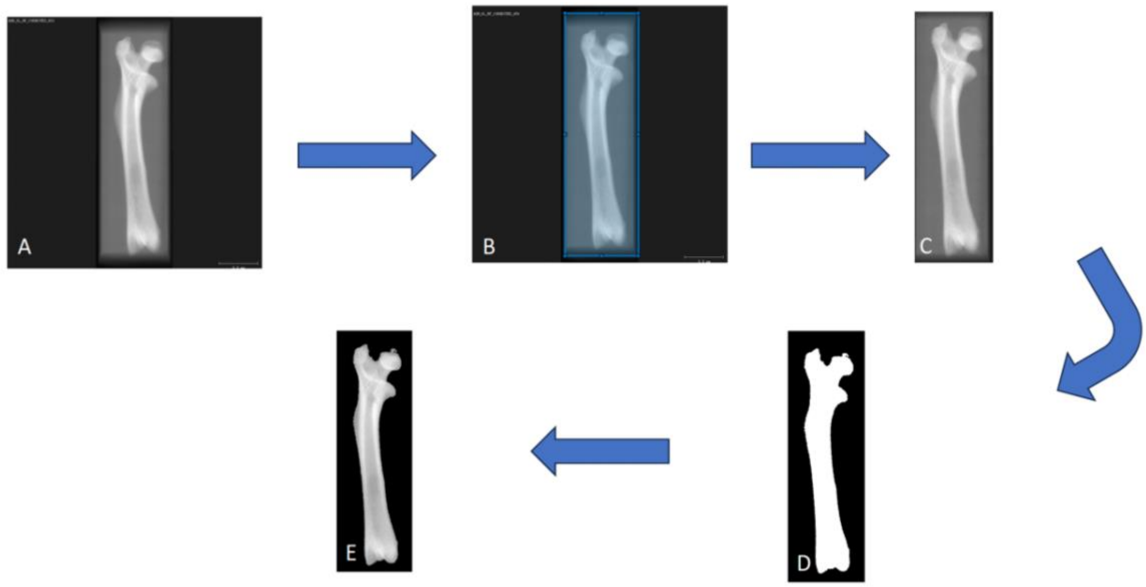

Figure 18. A: The original X-ray dicom of a rat femur, B: ROI is created to reduce computational time, C: Post ROI image processing, D: creating binary mask to remove surrounding white noise, E: binary mask is multiplied to original grayscale resulting in final bone structure.

4.2.2 Calculating Bone Mineral Density (BMD) from biplanar radiographs.

As mentioned in section 4.2 the amount of bone in each pixel is converted into an ‘areal density’’ which is measured in g/cm^2. The number of pixels in area is summoned which results in final bone mineral density of Xray of a femur.

Chapter 5

3-Dimensional Reconstruction for Rigidity Analysis

5.1. Introduction to Reconstruction Techniques

Until recently, the physicians have had at his disposal only a few means of gaining information about the 3-dimensional location and arrangement of normal or diseased organs and tissues with his patient's body. The sense of touch, conventional X-ray pictures, radioactive tracers and exploratory surgery are all useful but have limitations. In recent years the practice of medicine is entering an era in which the internal structures of body are being made far more accessible by non-invasive procedures. These may affect a revolution in medicine comparable to that brought in late 19th centaury by the introduction of anesthetics and sterile techniques. One particular noninvasive technique is called reconstruction from Projections, is coming to service in hospitals throughout the world. This technique involves mathematically combining X-ray images made from numerous angles into images in three dimensions of the organs within the body.

In conventional radiography X rays diverge from a source and pass through body, projecting an image of bones, organs, air spaces and any existing tumors onto the sheet of film. Invaluable though the procedure it, it suffers from a major short coming: there are overlaps of a structure on film due there is no significant difference between the X-ray density of one subject from another.

In attempting to surmount this shortcoming the physician often makes a number of X-ray pictures from different angles, in which the internal organs appear in different relationships to one another. This qualitative procedure is now being replaced by the new quantitative, mathematical technique that combines X-ray pictures to yield a representation of the internal structure in three dimensions. With such vital information available diagnosis becomes more accurate, and more precise guidance can be given to the hand of the surgeon and to therapeutic radiation aimed at a tumor.

The mathematical methods for reconstructing images from projections are being applied in a broad range of endeavors outside medicine. For example, in microscopy and in industrial nondestructive testing three-dimensional internal structure has been reconstructed from projected images made not only with X rays but also with light, electrons and protons. In astronomy similar methods are used to reconstruct images in two dimensions of celestial objects from their radio and X-ray signals.

5.2 Tailored Reconstruction Method

Once the background noise is removed as shown in figure 17, AP and Lateral projections are converted into grayscale version. For this case, we are assuming femur to be an oblique circular cylindrical structure which has an elliptical cross section. Distance between first and last pixel is calculated for the AP and lateral projection which serves as the major and minor axis of ellipse. These values are later used to plot the ellipse. This method is followed for every rows. By plotting every row, it is possible to reconstruct the outer surface of a femur. The outer surface of femur is shown in Figure 19.

Figure 19: The outer surface of a femur

To see the accuracy of the reconstructed femur AP projection and Lateral Projection was developed as shown in Figure 20.

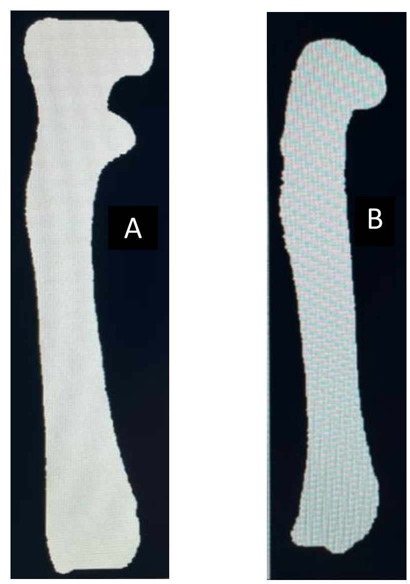

Figure 20: (a) AP projection of reconstructed femur, (b) Lateral Projection of reconstructed femur

5.2.1 3-Dimensional Reconstruction of all surfaces of Femur

Once the outer surface is reconstructed, now the developed algorithm reads all the successive inner surfaces from the grayscale image, and it reconstructs a 2-Dimensional surface from grayscale elements. An example Matrix is shown below in figure 21 which gives detailed insight of working principle of reconstruction algorithm. Suppose the example grayscales are:

AP = [10, 20, 30, 40, 50, 35,40;
0, 70, 80, 90, 10, 56, 0;
0, 0, 78, 98, 65, 0, 0;
0, 64, 87, 98, 34, 76, 0].

LAT = [90, 70, 10, 60, 87;
0, 80, 80, 23, 10;
0, 20, 30, 40, 0;
0, 70, 32, 65, 0]

Table 3 includes the information needed for reconstruction of the first row and table 4 includes the information needed for reconstruction of row 2.

Table 3: Length of major and minor axes for row 1

Surface	Length of Major Axis	Length of Minor Axis
1	7	5
2	5	3
3	3	1
4	1	1

Table 4: Length of major and minor axes for row 2

Surface	Length of Major Axis	Length of Minor Axis
1	5	4
2	3	2

This process is repeated for all the rows of biplanar projections and then the values of major and minor axis are used as an input for equation 11:

$$\frac{x^2}{a^2} + \frac{y^2}{b^2} = 1 \tag{11}$$

Where a is length of major axis and b is length of minor axis.

Figure 21 and figure 21 depicts the reconstructed row 1 and 2.

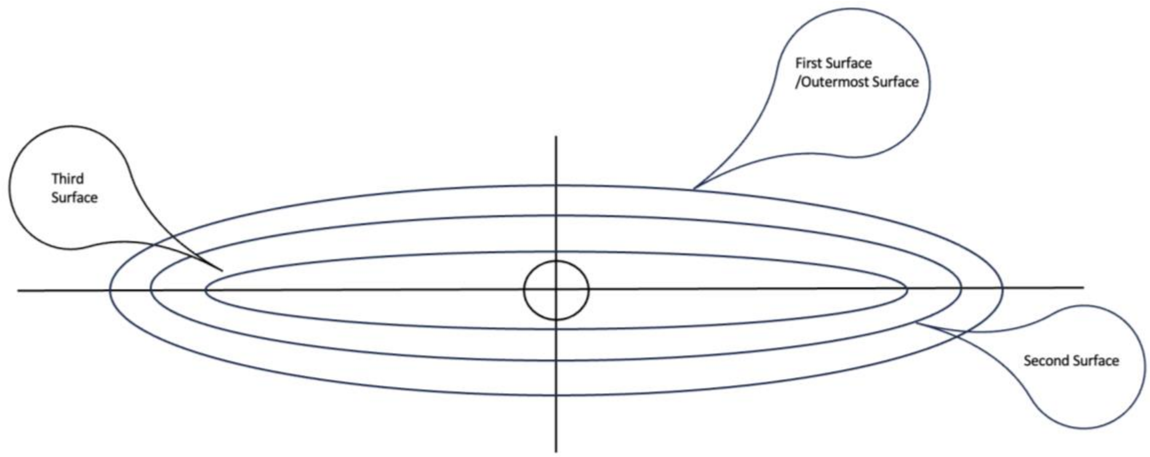

Figure 21: Reconstruction of first row from above example matrix

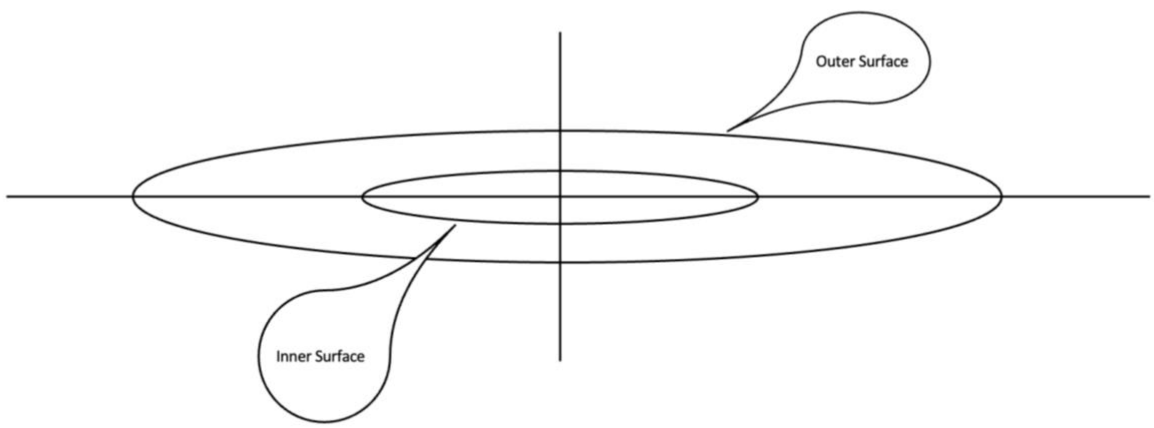

Figure 22: Reconstruction of second row from example matrix

5.3 Linear Interpolation to predict the values of individual pixel density of reconstructed surfaces

Standard Linear Interpolation which dates back to Babylonians [lxxii] is by far the most popular solution for computer applications such as computer vision, digital photography, computer graphics and image calibration. It helps in building new data points within the range of a discrete set of already known data points. Therefore, the Linear interpolation is the simplest method for estimating a channel from the vector of the given channel's estimates. Linear interpolation is useful while searching for a value between given data points. Therefore, mathematician considers it as "filling in the gaps" for a given data values in tabular format. The strategy for linear interpolation is to use a straight line to connect the given data points on positive as well as the negative side of the unknown point.

The simplest Interpolation formula can be given as

$$\frac{y-y_0}{x-x_0} = \frac{y_1-y_0}{x_1-x_0}, \tag{12}$$

Where the known pixel densities are given by (x_0, y_0) and (x_1, y_1), the linear interpolant s the straight line between these two points. This formula can also be understood as a weighted average. The weights are inversely related to distance from the end points to unknown points; the closer point has more influence than farther point.

The interpolated values are then integrated with the reconstructed surface which yields a 3-dimensional model of a femur which can predict the shape of a bone as well as pixel densities at any given location. Figure 23 shows the final bone model in a 3-Dimensional plane.

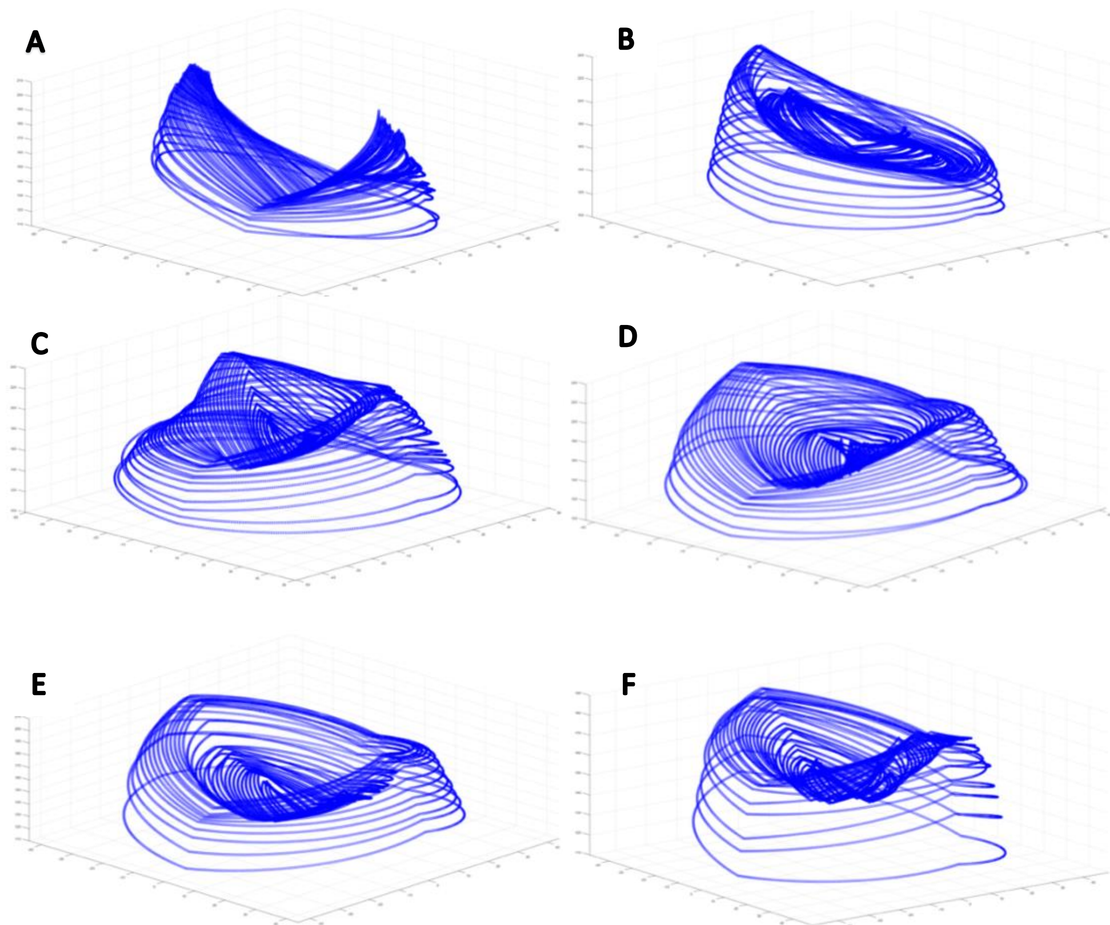

Figure 23: 3-dimensional model of a femur from biplanar radiographs

5.4 Validation of 3-Dimensional Model against biplanar radiographs

For the ease of computational complexities, pixel densities from every 100th row of biplanar radiographs are plotted and they are compared with every 100th surface of 3-Dimensional reconstructed femur to see how closely the model resembles to biplanar radiographs.

5.4.1 Comparing 100th row from biplanar radiograph with 100th surface from 3-Dimensional reconstructed femur

Individual pixel density was plotted for the biplanar radiograph, and it is compared against the 100th surface of 3-Dimensional reconstructed surface as shown in figure 24.

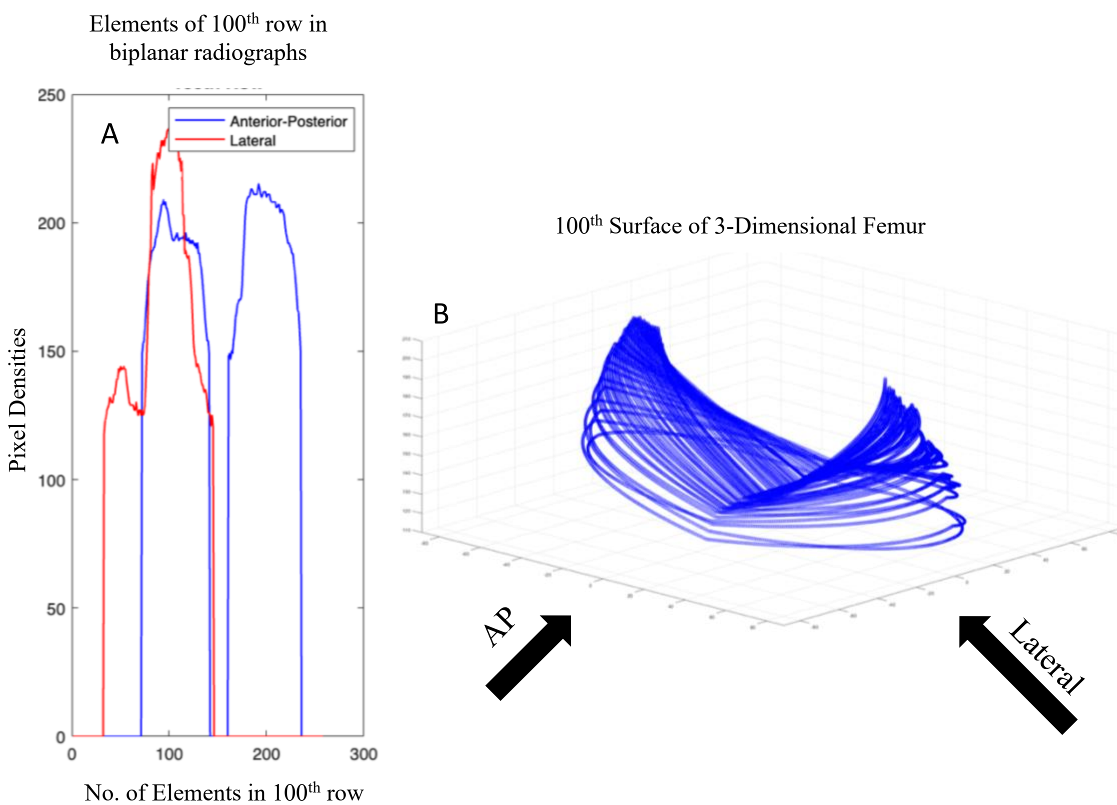

Figure 24: (a) Pixel Densities of elements in 100th row of biplanar projections, (b) 100th surface of 3-Dimensional reconstructed femur

As seen in the 2-D plot of biplanar radiographs, the peaks of AP are achieved near the periphery of femur and there is a sharp dip in the middle, a similar trend can be observed in 3-D model.

5.4.2 Comparing 200th row from biplanar radiograph with 200th surface from 3-Dimensional reconstructed femur

Individual pixel density was plotted for the biplanar radiograph, and it is compared against the 200th surface of 3-Dimensional reconstructed surface as shown in figure 25.

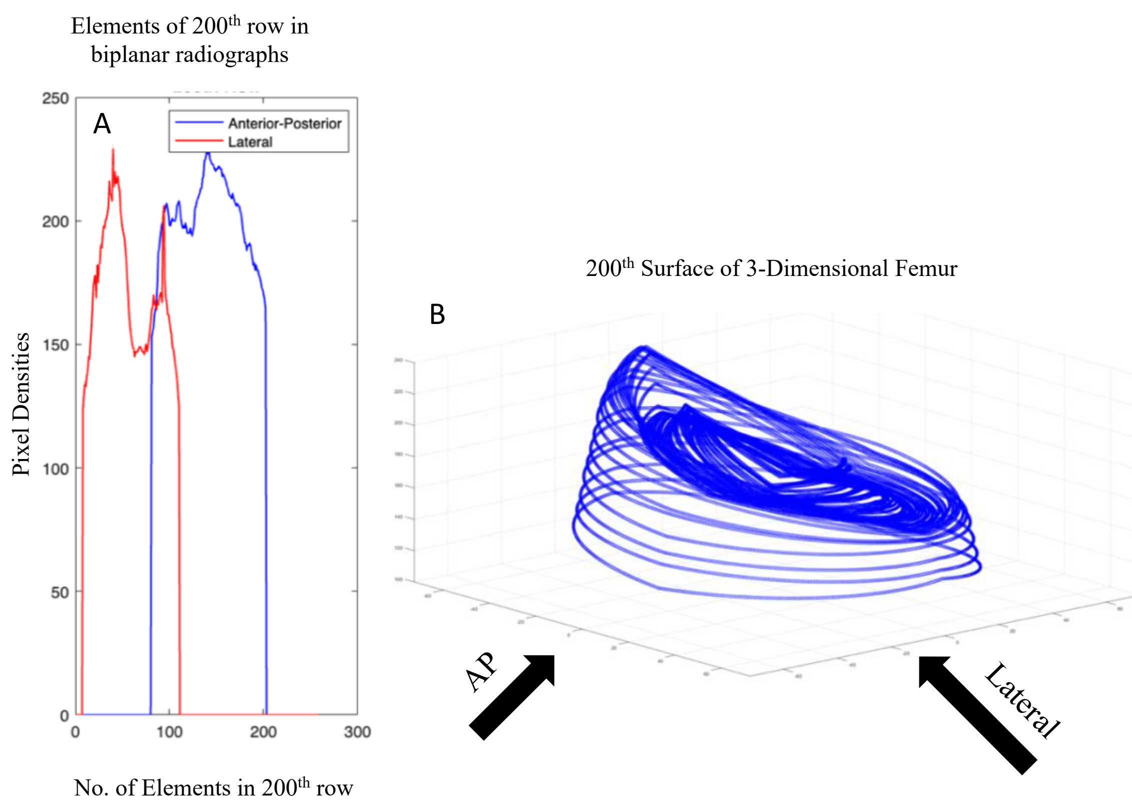

Figure 25: (a) Pixel Densities of elements in 200th row of biplanar projections, (b) 200th surface of 3-Dimensional reconstructed femur

As seen in the 2-D plot of biplanar radiographs, there is no significant dip observed in biplanar radiographs, a similar trend can be observed in 3-D model.

5.4.3 Comparing 300th row from biplanar radiograph with 300th surface from 3-Dimensional reconstructed femur

Individual pixel density was plotted for the biplanar radiograph, and it is compared against the 300th surface of 3-Dimensional reconstructed surface as shown in figure 26.

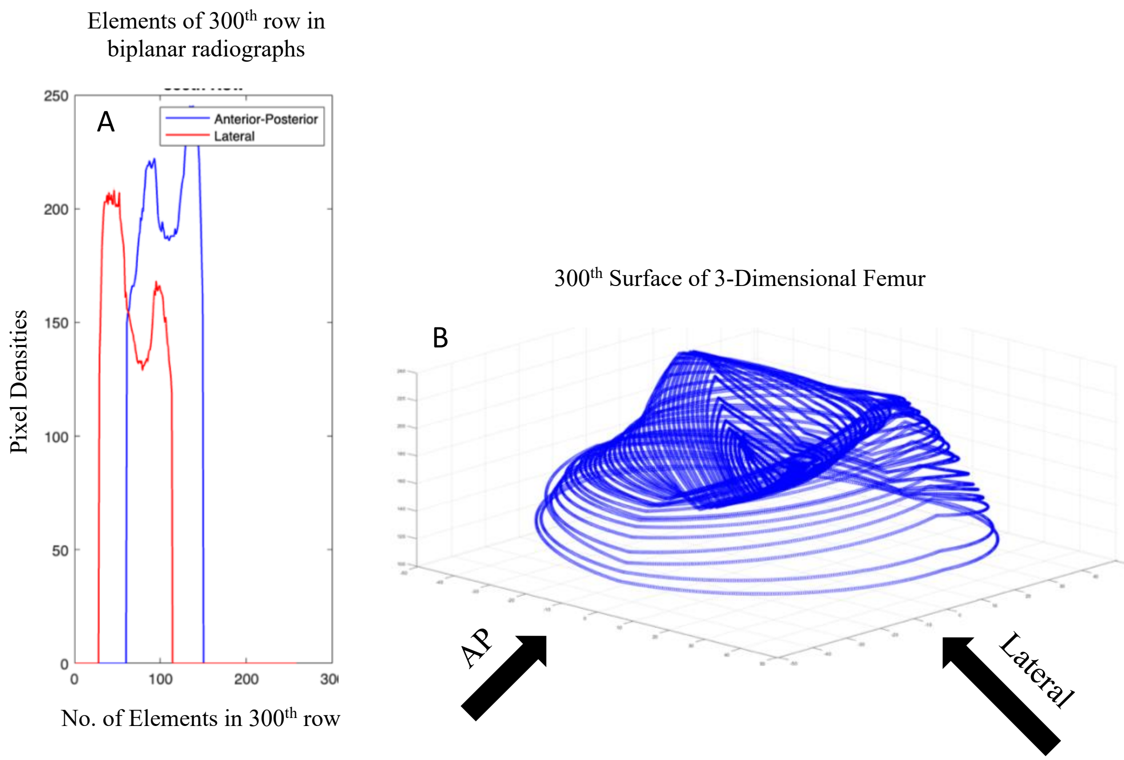

Figure 26: (a) Pixel Densities of elements in 300th row of biplanar projections, (b) 300th surface of 3-Dimensional reconstructed femur

A significant relevance can be seen amongst 2-D biplanar graph and 3-D model.

5.4.4 Comparing 400th row from biplanar radiograph with 400th surface from 3-Dimensional reconstructed femur

Individual pixel density was plotted for the biplanar radiograph, and it is compared against the 400th surface of 3-Dimensional reconstructed surface as shown in figure 27.

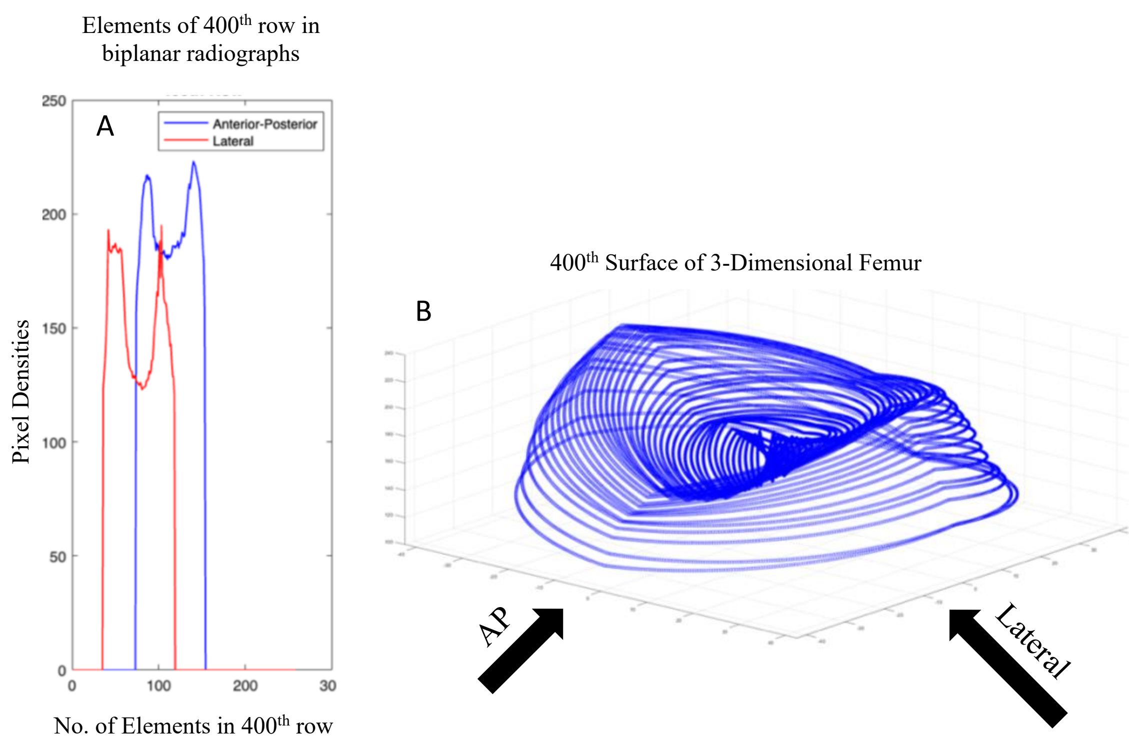

Figure 27: (a) Pixel Densities of elements in 400th row of biplanar projections, (b) 400th surface of 3-Dimensional reconstructed femur

As seen in the 2-D plot of biplanar radiographs, the peaks of AP are achieved near the periphery of femur and there is a sharp dip in the middle indicating the trabecular bone, a similar trend can be observed in 3-D model.

5.4.5 Comparing 500th row from biplanar radiograph with 500th surface from 3-Dimensional reconstructed femur

Individual pixel density was plotted for the biplanar radiograph, and it is compared against the 500th surface of 3-Dimensional reconstructed surface as shown in figure 28.

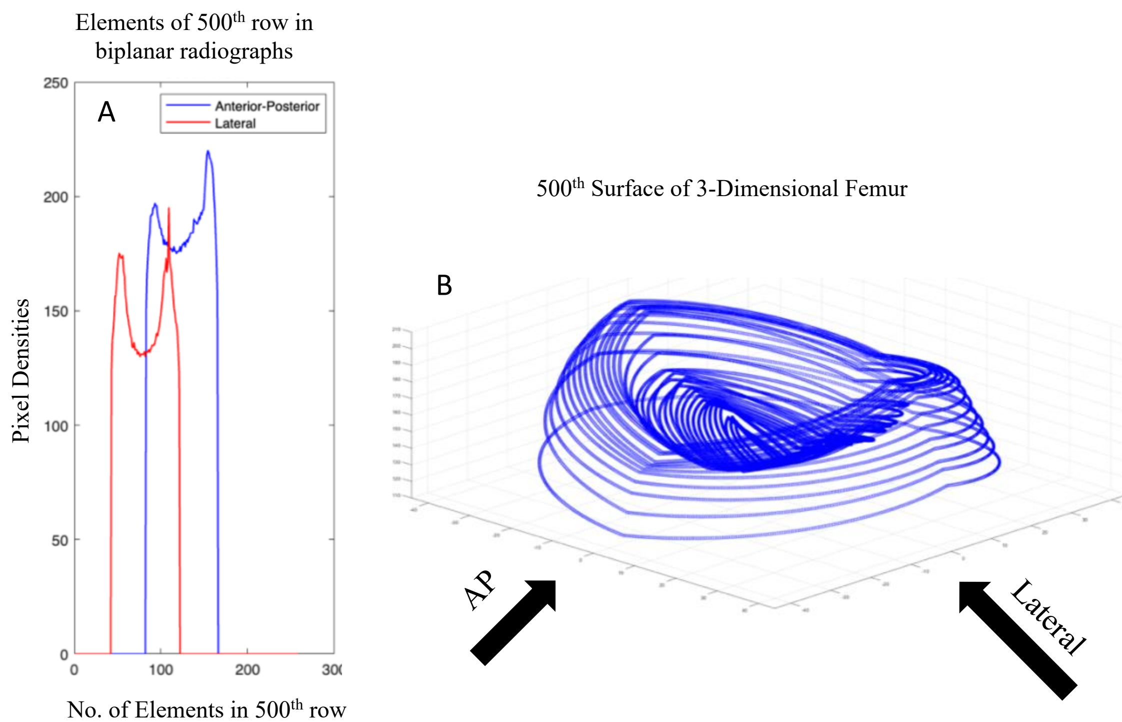

Figure 28: (a) Pixel Densities of elements in 500th row of biplanar projections, (b) 500th surface of 3-Dimensional reconstructed femur

5.4.6 Comparing 600th row from biplanar radiograph with 600th surface from 3-Dimensional reconstructed femur

Individual pixel density was plotted for the biplanar radiograph, and it is compared against the 600th surface of 3-Dimensional reconstructed surface as shown in figure 29.

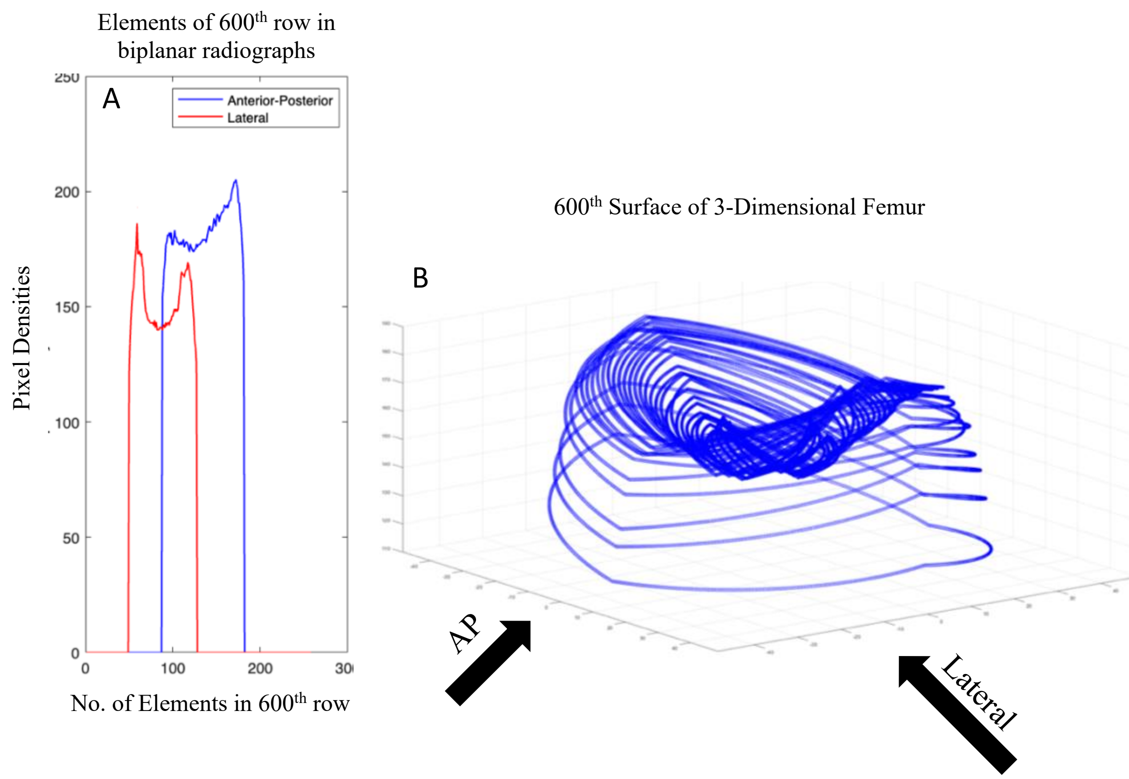

Figure 29: (a) Pixel Densities of elements in 600th row of biplanar projections, (b) 600th surface of 3-Dimensional reconstructed femur

Chapter 6

Rigidity Analysis

The beam, or flexural member, is frequently encountered in structures and machines, and its elementary stress analysis constitutes one of the more interesting facets of mechanics of materials. A beam is a member subjected to loads applied transverse to the long dimension, causing the member to bend. For example, a simply supported beam loaded at its third points will deform into the exaggerated bent shape shown in Fig. 31

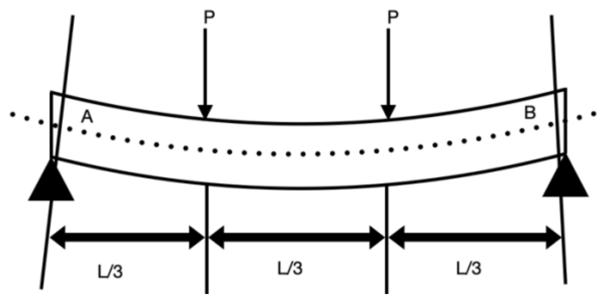

Fig 30: Simply supported beam loaded at its third points.

Beams are frequently classified on the basis of supports or reactions. A beam supported by pins, rollers, or smooth surfaces at the ends is called a simple beam. A simple support will develop a reaction normal to the beam but will not produce a moment at the reaction. The femur is assumed to be a simple beam. Rigidity is a structural property that integrates both the material and geometric properties of bone; the axial (EA), bending (EI) and torsional (GJ) rigidities determine the capacity of the bone to resist axial, bending and twisting loads, respectively. We submit that the structural rigidity of a bone afflicted with distraction osteogenesis provides a mechanical assay that represents the changes in tissue material and geometric properties induced by the disease. Based on the principle that it is the weakest section that dictates the load capacity for the entire bone, we have developed algorithms to calculate the minimal rigidity of a bone with a neoplastic lesion from biplanar radiographs to measure bone mineral density and cross-sectional geometry, referred to as X-ray based structural rigidity Analysis.

As plain radiographs are routinely obtained when treating patients' investigators have tried to estimate the load-bearing capacity (LBC) of a bone from simple radiographic measurements [lxxiii]. Radiographic criteria that rely on measuring defect size only account for the geometry of the defect. However, geometric characterizations of lytic lesions alone do not accurately predict the risk of fracture [lxxiv]. Furthermore, these criteria do not take into consideration the loading mode or the relative location of the defect. The mechanical behavior of a structure is a function of its material and geometric properties; any method of fracture risk prediction must be able to measure changes in both bone material behavior and bone structural geometry. Current imaging techniques are capable of noninvasive measurements of bone density and cross-sectional geometry. These data, in conjunction with composite beam theory, can be used to predict the LBC of bones with lytic defects. Composite beam theory is an analytical theory that accounts for both the material properties of the individual elements that make up a structure and the overall geometry of the structure itself. Such an approach allows for the estimation of bone structural rigidity, a property defined by the product of the material modulus (which is treated as a function of bone density) and cross-sectional geometry of the structure, and it is equivalent to the slope of the linear portion of the load-deformation curve.

In practice, biplanar radiographs of involved bones are obtained it is then converted to its grayscale and processed through image processing algorithm as mentioned in previous chapters. To estimate 3-dimensional shape of a bone, reconstruction algorithm was developed which thresholds trabeculae components of femur, and it calculates distance between the first and the last pixel is calculated for every row of AP and Lateral projections of biplanar radiographs. These distances serve as major and minor axis of ellipse. The geometric composition of cortical bone is estimated by the geometry of ellipse as shown in figure 32. Finally, to estimate the composition in each slides linear interpolation was used.

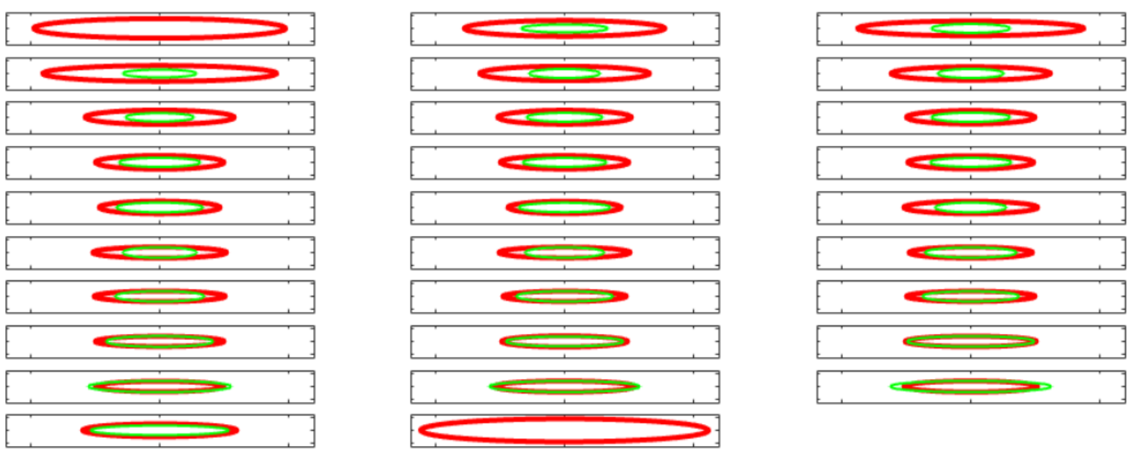

Fig 31: 3-dimensional shape of femur using biplanar radiographs

Furthermore, the reconstructed images are transformed to be perpendicularly aligned to the neutral axis of the bone of interest in order to obtain true 3-dimensional images. For each reconstructed image, EA, EI and GJ are calculated by summing up the modulus-weighted area of each pixel within the bone contour by the position of the pixel relative to the centroid of the bone cross-section. In these three rigidities, E is the modulus of elasticity (Young's modulus) of the trabecular or cortical bone, A is the cross-sectional area of the reconstructed bone section under consideration, I is the second moment of inertia, G is the torsional modulus of the trabecular or cortical bone and J is the polar moment of inertia. EA provides a measure of the bone's resistance to uniaxial loads; EI provides a measure of the bone's resistance to bending moments; and GJ provides a measure of the bone's resistance to torsional loads.

The moment of inertia (I) is a tensor; therefore, its magnitude depends on the orientation of the bone cross-section relative to the direction of the applied bending moment. To account for this, we solve the eigenvalue problem and determine the principal values Imax and Imin. Assuming a worst-case scenario, we use the minimum principal value, Imin, when tabulating the bending rigidities for each sequential cross-section through the bone.

The location of the modulus weighted centroid (figure 32), which is assumed to be the neutral bending axis, is first corrected to account for the curvature of the femoral neck. The location (coordinates) of the neutral bending axis is first corrected to account for the composite of bone elastic moduli distributed in the cross-section and then for the radius of curvature of the

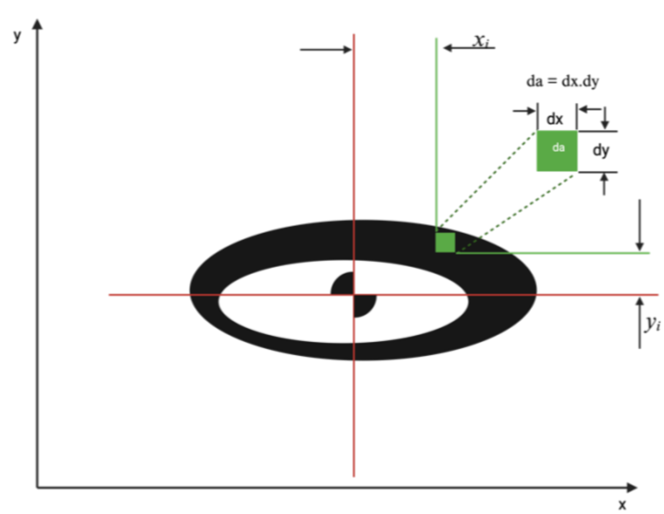

Figure 32: Axial (Ea), Bending (Ei), and Torsional (Gj) rigidities were calculated, with the use of indicated algorithm

femoral neck in the coronal plane corresponding to that cross-section. Modeling each sequential transaxial cross-section of bone as an independent beam element and invoking Castigliano's second theorem, we assume that the cross-section through the bone with the minimum EA, EI and GJ governs the load bearing capacity of the entire bone for the corresponding loading mode.

The density (ρ) of each pixel corresponding to bone was calculated from the biplanar radiographs individual pixel values to the mineral bone density. The modulus of elasticity of femur was derived using Cory et. al.[lxxv] relationship:

$E = 8362.8({\rho_{EQUIV}}^{2.56})$

EA, EI and GJ were calculated using the following formulae:

$$EA = \int E(\rho)da \tag{13}$$

$$EI = \int E(\rho)y^2 da \tag{14}$$

$$GJ = \int G(\rho)(x^2 + y^2)da \tag{15}$$

where x and y are the distances to the neutral axis of the trans axial cross-section, and da is the pixel area.

The cross-section through the affected bone that had the lowest rigidity was considered the weakest link and was assumed to govern the failure behavior of the entire bone. However, this does not mean that the software tool can predict the exact failure load or pinpoint the exact location of an impending fracture. On the contrary, this developed software tool seeks to determine a fracture risk threshold whole bone using simple and reproducible measures.

Chapter 7

Validation and Results

7.1 Validation of BMD from developed machine learning model against Micro-CT imaging modality.

Comparison of BMD from developed machine learning algorithm with BMD from Micro-CT reveals a strong relationship between imaging modalities (table 5). The comparison of regression analyses (figure 33) based on the provided graph reveals significant insights. With an impressive coefficient of determination (R-squared) of 0.88, the depicted dataset demonstrates a remarkably strong relationship between the BMD from uCT and BMD from biplanar radiographs. This high R-squared value suggests that approximately 88% of the variability in the BMD from biplanar radiographs can be explained by the BMD from uCT, indicating a robust fit of the regression model. Furthermore, the graph depicts a tightly clustered distribution of data points around the regression line, indicating minimal residual variability and adherence to assumptions of normality and homoscedasticity. Consequently, this dataset exhibits a compelling case of a well-fitted regression model with substantial predictive power.

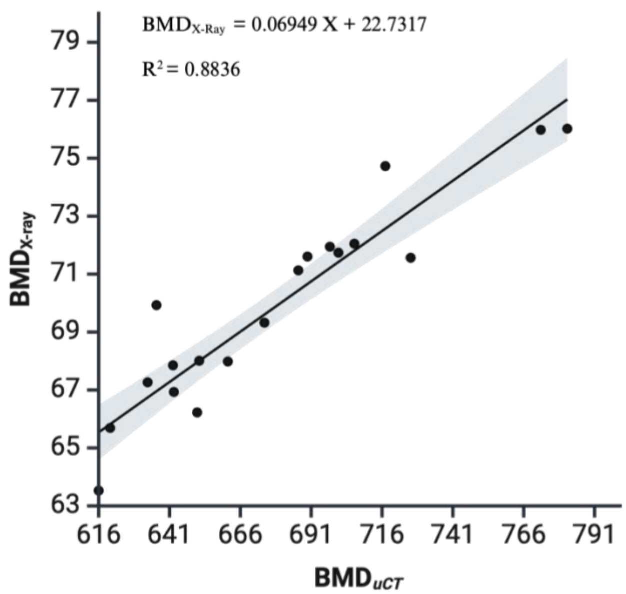

Figure 33: The slope of regression line for correlation between BMD measure from uCT and the predicted BMD using machine learning model

Table 5: Comparing BMD from Micro-CT and Machine learning algorithm

Sample No.	BMD (uCT)	Unit (uCT)	BMD (X-ray)	Unit (X-ray)
1	689.6846	[mg HA/ccm]	71.6057	(g/cm^2)
2	700.6121	[mg HA/ccm]	71.7395	(g/cm^2)
3	697.594	[mg HA/ccm]	71.9455	(g/cm^2)
4	781.371	[mg HA/ccm]	76.0187	(g/cm^2)
5	616.0025	[mg HA/ccm]	63.5279	(g/cm^2)
6	661.5855	[mg HA/ccm]	67.9839	(g/cm^2)
7	642.5405	[mg HA/ccm]	66.9324	(g/cm^2)
8	686.4584	[mg HA/ccm]	71.13	(g/cm^2)
9	642.2283	[mg HA/ccm]	67.8518	(g/cm^2)
10	651.4907	[mg HA/ccm]	68.0095	(g/cm^2)
11	613.6089	[mg HA/ccm]	64.6422	(g/cm^2)
12	674.4903	[mg HA/ccm]	69.3242	(g/cm^2)
13	620.0613	[mg HA/ccm]	65.6896	(g/cm^2)
14	726.1094	[mg HA/ccm]	71.5649	(g/cm^2)
15	706.2319	[mg HA/ccm]	72.05	(g/cm^2)
16	717.1593	[mg HA/ccm]	74.73	(g/cm^2)
17	633.2783	[mg HA/ccm]	67.2653	(g/cm^2)
18	636.4004	[mg HA/ccm]	69.93	(g/cm^2)
19	650.7621	[mg HA/ccm]	66.2263	(g/cm^2)
20	772.0046	[mg HA/ccm]	75.98	(g/cm^2)

7.2 Validating EI_{min} from X-rays against Micro-CT Imaging

The test was run on 7 samples for axial (EA), bending (EI) and torsional rigidities (GJ) for each transaxial cross-section image are calculated by summing the modulus-weighted area of each voxel comprising the bone section by its position relative to the centroid of the bone. Axial rigidity provides a measure of the bone's resistance to deformation when subjected to uniaxial loads. Bending rigidity provides a measure of the bone's resistance to bending deformation when subjected to bending moments. Torsional rigidity provides a measure of the bone's resistance to twisting deformation when subjected to torsional moments. The moment of inertia (I) is a tensor; therefore, its magnitude depends on the orientation of the bone cross-section relative to the direction of the applied bending moment. To account for this, we solve the eigenvalue problem and determine the principal values Imax and Imin. Assuming a worst-case scenario, we use the minimum principal value, Imin, when tabulating the bending rigidities for each sequential cross-section through the bone.

Although rigidity analysis was performed on entire length of femur, for results only the regions from greater trochanter to supracondylar ridge was taken into consideration for numerous reasons. According to Brody-Camp et. al[lxxvi] D.O. is a surgical procedure which takes place in regions where the concentration of cortical bone is higher. Following the suggestion, proximal and distal ends of femur were disregarded. A univariate power law regression revealed that rigidities can calculated from biplanar radiographs to quantify bone growth during distraction osteogenesis ($R^2 = 0.78 - 0.91$) as shown in figure 35.

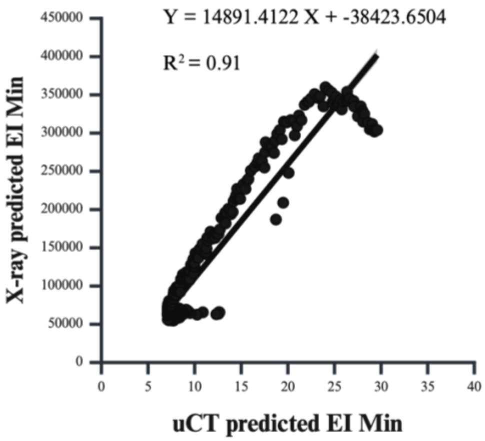
Y = 14891.4122 X + -38423.6504
$R^2 = 0.91$
X-ray predicted EI Min
uCT predicted EI Min

A

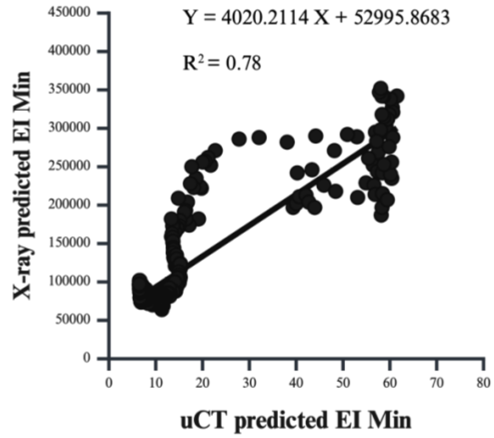
Y = 4020.2114 X + 52995.8683
$R^2 = 0.78$
X-ray predicted EI Min
uCT predicted EI Min

B

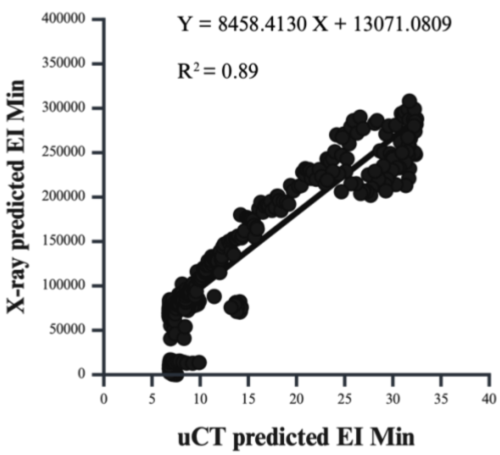
Y = 8458.4130 X + 13071.0809
$R^2 = 0.89$
X-ray predicted EI Min
uCT predicted EI Min

C

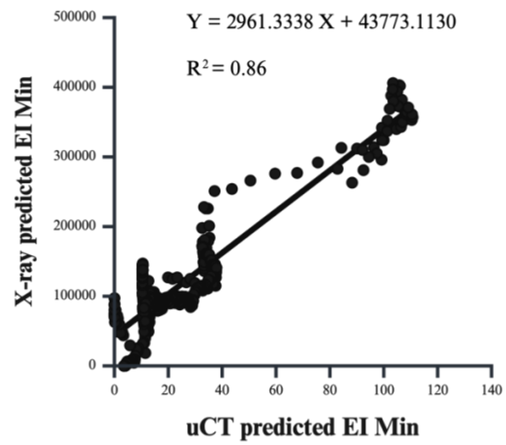
Y = 2961.3338 X + 43773.1130
$R^2 = 0.86$
X-ray predicted EI Min
uCT predicted EI Min

D

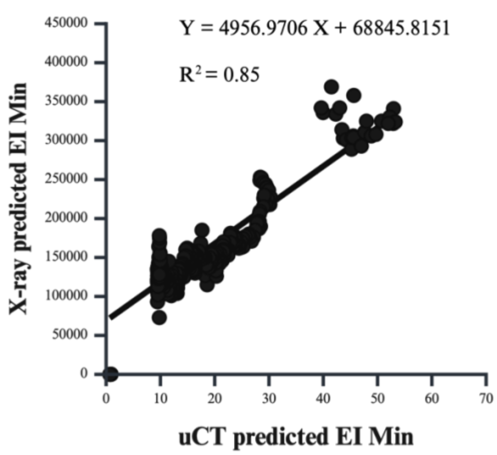
Y = 4956.9706 X + 68845.8151
$R^2 = 0.85$
X-ray predicted EI Min
uCT predicted EI Min

E

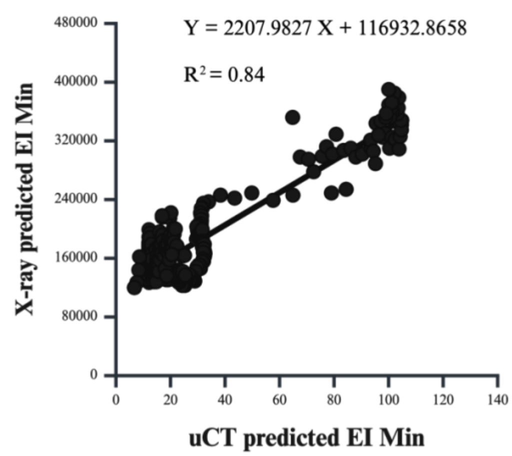
Y = 2207.9827 X + 116932.8658
$R^2 = 0.84$
X-ray predicted EI Min
uCT predicted EI Min

F

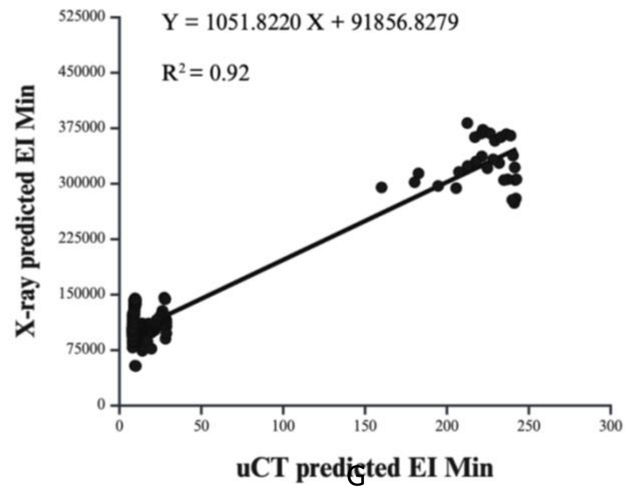

G

Figure 34: Regression model comparing I_{min} from micro-CT against X-ray

Chapter 8

Discussion

Presented in this thesis is an algorithm pipeline that can predict axial (EA), bending (EI) and torsional rigidities (GJ) for each reconstructed trans axial cross-section from biplanar radiograph, that are calculated by summing the modulus-weighted area of each voxel comprising the bone section by its position relative to the centroid of the bone.

The moment of inertia (I) is a tensor; therefore, its magnitude depends on the orientation of the bone cross-section relative to the direction of the applied bending moment. To account for this, we solve the eigenvalue problem and determine the principal values Imax and Imin. Assuming a worst-case scenario, we use the minimum principal value, Imin, when tabulating the bending rigidities for each sequential cross-section through the bone.

The location of the modulus weighted centroid, which is assumed to be the neutral bending axis, is first corrected to account for the curvature of the femoral neck. The location (coordinates) of the neutral bending axis is first corrected to account for the composite of bone elastic moduli distributed in the cross-section and then for the radius of curvature of the femoral neck in the coronal plane corresponding to that cross-section. Modeling each sequential reconstructed transaxial cross-section of bone as an independent beam element and invoking Castigliano's second theorem, we assume that the cross-section through the bone with the minimum EA, EI and GJ governs the load bearing capacity of the entire bone for the corresponding loading mode.

By using this approach, the predicting accuracy is not compromised at any stage during measurements. Numerous tests were run from initial to final stage to check efficacy of software. The software is discretized in 5 parts. In the first stage, an image processing algorithm reads dicom from biplanar radiographs and it automatically decides the region of interest. Once ROI is defined, global threshold is calculated by software to get rid of lens flare. It is important to note that threshold intensity is decided by software to reduce on human inputs.

Once the bone is separated from surrounding noise a BMD algorithm is initiated. It predicts the mineral density from biplanar radiographs. An impressive correlation was observed between BMD predicted from gold standard and developed algorithm.

In 3rd phase of the software, to overcome the limitations of a traditional biplanar radiographs and Dual-Energy Xray Absorptiometry (DEXA) a reconstruction algorithm is initiated once BMD is predicted. The reconstruction algorithm reads grayscale of biplanar radiographs, and it determines length of major and minor axes from AP and Lateral projection for each row. For every row, the software first reconstructs the outer surface and then inner surfaces are calculated successively. Following this method, it allows to predict a 3-Dimensional shape of a bone. However, in this work there few drawbacks in predicting shape of femoral head and femoral neck due to complex orientation and shape. However, since distraction osteogenesis is a procedure which is performed in regions where presence of cortical bone is dominant, so proximal femur wasn't taken into consideration in final result.

Till 3rd phase, software can successfully predict 3-Dimensional shape of bone from biplanar radiographs. However, it still lacks in predicting material properties of bone. By predicting material properties, for every trans axial slide of reconstructed bone would allow to differentiate between micro-architecture compositions of bone. Current standard of care is mapping cortices ≥ 2mm or thick in distracted segment. Moreover, the inter-observer agreement is less than 50%. Currently there are no measures to *quantify* bone growth in distracted region. As a result, it leads to fractures even after successful completion of surgery. To address above mentioned limitations, the primary step is to predict the microarchitecture of a bone from biplanar radiographs.

In 4th stage, a linear interpolation algorithm was developed to predict bone composition of every voxel in 3-Dimensional reconstructed bone from biplanar radiograph projections. Following this approach, material properties can be predicted across the entire length of bone. Not only materials properties can be estimated, but also just like a Computed Tomographic (CT) scan, microarchitecture of a subjected bone can be easily differentiated.

In 5th stage, a rigidity analysis algorithm was developed which calculates rigidity of input dicom files. Axial (EA), Flexural (EI) and Torsional (GJ) rigidities were calculated for each trans axial images.

A regression analysis was performed for 7 samples which were selected for test. An impressive R^2 value was observed ranging from 0.78 to 0.92, indicating a strong relationship between values of EI_{min} from 3-Dimensional Reconstructed femur from biplanar radiographs with values of EI_{min} from Micro-CT scans.

Lastly, to avoid human error at any stage of analysis, the entire algorithm was programmed to predict values of human dependent parameters like thresholding intensity at every stage on its own. As a result of automizing these steps, overpredicting or underpredicting any microarchitecture of bone in predicting BMD, EA, EI and GJ is eliminated.

Chapter 9

Limitations

The primary limitation in the current iteration of the software lies in its inability to accurately forecast the three-dimensional shape towards the proximal and distal ends of the femur. This discrepancy arises due to the intricate geometries of the bone, particularly within the femoral neck region. Currently, the software is tailored for application in distraction osteogenesis settings. However, through refined modeling techniques, we will broaden the software's capabilities to encompass a wider spectrum, specifically targeting fracture healing.

Chapter 10

Conclusions and Future Work

10.1 Conclusions

In this thesis, it has been proved that biplanar radiographs can predict 3-Dimensional shape and microarchitecture of a bone. X-rays cheap, accessible and it uses less radiation than a computed tomographic scan. Moreover, the material predictive capabilities of a bone are not compromised even after significantly reducing radiation doses. As a result of reduced doses, the application bandwidth of developed software increases to areas where previously it was not possible without a computed tomographic scan.

There is an unmet clinical need to better identify which patients are at substantial fracture risk, so that appropriate intervention can be initiated before catastrophic failure occurs. Currently, there is no proven sensitive or specific method for predicting rigidity of regenerated bone in distracted segment. Decisions regarding the management of bone lesions are currently based on geometric measurements of the bone, the defect or both. The results of several studies suggest that better treatment plans can be made by predicting failure (and, by extension, by predicting fracture).

The load-carrying capacity of bone depends on many factors that are not represented by radiographic criteria based on lesion size alone. The critical parameters that determine the LBC of a bone containing a lytic lesion include the amount of bone loss, the cross-sectional structural geometry of the bone, the material properties of the remaining bone tissue, the location of the lesion with respect to the applied loads and the loading mode. Software presented in this thesis uses rigidity is used as a mechanical assay to accurately predict the load bearing capacity of bone. We have developed an accessible, point of care technology, X-ray based Rigidity Analysis solution, which utilizes low radiation, biplanar radiographic projections, through healing and pathologic bone to predict its load bearing capacity and failure risk based on calculating the minimal axial, bending, and torsional rigidities.

The advantage of our analysis of structural rigidity with biplanar radiographs is that it reflects changes in both the material properties of the bone tissue and the bone cross-sectional geometry for any bone or lesion. BMD alone, which is often used to predict the risk of poorly developed distracted bone fragment, does not reflect how the bone mineral is distributed in space, which determines the load-carrying capacity of the bone.

X-ray based rigidity analysis is a potential, robust, and noninvasive tool, based on fundamental principles of engineering mechanics, and can be used to reliably identify patients at risk of poor bone formation in distracted segments. However, and because of the novelty of the technique, there are no clinical guidelines or criteria to determine efficacy of regenerated bone in distracted segment. Increased awareness of clinicians to X-ray based rigidity analysis, including its underlying methodology to study bone structural characteristics, may establish this methodology as a uniform guideline across specialties to assess fracture risk and to plan treatment for patients afflicted with osseous lesions.

10.2 Future Work

One limitation in current version of software is its inaccuracy in predicting 3-Dimensional shape towards the proximal and distal end of femur. This takes place as a result of extremely complex geometries of bone towards femoral neck. Moreover, the transition from cortical to trabecular bone takes place in proximal and distal end of femur.

In order to address this issue, there is a need of better image reconstruction algorithm in 4^{th} stage which can mimic entire shape of femur accurately. Clinical studies can be performed once the reconstructed femur closely relates to original femur.

There is a need to perform distraction osteogenesis on a rabbit model to validate the software in live clinical conditions to investigate how closely a regenerated bone in distracted segment can be validated using its biplanar radiographs projections.

A retrospective study can also better help understand feasibility of software presented in this study.

References

[i] Hamdy, R. C., Rendon, J. S. & Tabrizian, M. Distraction osteogenesis and its challenges in bone regeneration. In *Bone Regeneration* (ed. Tal, H.) Ch. 8, 177–204 (InTech, 2012)

[ii] Dennis SC, Berkland CJ, Bonewald LF, Detamore MS. Endochondral ossification for enhancing bone regeneration: converging native extracellular matrix biomaterials and developmental engineering in vivo. *Tissue Engineering. Part B, Reviews* 2015 Jun;21(3):247–266.

[iii] Yang S, Wang N, Ma Y, Guo S, Guo S, Sun H. Immunomodulatory effects and mechanisms of distraction osteogenesis. *International Journal of Oral Science* 2022 Jan 24;14(1):4. doi: 10.1038/s41368-021-00156-y

[iv] Weinzweig J. *Plastic surgery secrets plus e-book. Chapter 31: principles of distraction osteogenesis.* Amsterdam: Elsevier; 2010. pp. 212–218

[v] Brody-Camp S, Winters R. Craniofacial Distraction Osteogenesis. [Updated 2023 Jul 24]. In: StatPearls [Internet]. Treasure Island (FL): StatPearls Publishing; 2023 Jan-. Available from: https://www.ncbi.nlm.nih.gov/books/NBK560915/

[vi] Shen Z, Lin H, Chen G, Zhang Y, Li Z, Li D, Xie L, Li Y, Huang F, Jiang Z. Comparison between the induced membrane technique and distraction osteogenesis in treating segmental bone defects: An experimental study in a rat model. *PLoS One.* 2019;14(12):e0226839.

[vii] Hierl T, Klisch M, Kloppel R, Hemprich A. Distraction osteogenesis in the treatment of severe midfacial hypoplasia. *Mund-, Kiefer-, und Gesichtschirurgie* 2003:7:7–13. https://doi.org/10.1007/s10006-002-0440-1

[viii] Mofid MM, Manson PN, Robertson BC, Tufaro AP, Elias JJ ,Vander Kolk CA. Craniofacial distraction osteogenesis : a review of 3278 cases. *Plastic and Reconstructive Surgery* 2001:108(5):1103–1114. https://doi.org/10.1097/00006534-200110000-00001

[ix] Suzuki EY, Motohashi N, Ohyama K. Longitudinal dento-skeletal changes in UCLP patients following maxillary distraction osteogenesis using RED system. *Journal of Medical and Dental Sciences* 2004:51(1):27–33.

[x] Swennen G, Schliephake H, Dempf R, Schierle H, Malevez C. Craniofacial distraction osteogenesis: a review of the literature: Part 1: clinical studies. *International Journal of Oral and Maxillofacial Surgery* 2001 Apr;30(2):89–103. doi: 10.1054/ijom.2000.0033

[xi] Raoul G, Wojcik T, Ferri J. Outcome of mandibular symphyseal distraction osteogenesis with bone-borne devices. *Journal of Craniofacial Surgery* 2009 Mar; 20(2):488–493. doi: 10.1097/SCS.0b013e31819b9d2c

[xii] van Strijen PJ, Breuning KH, Becking AG, Perdijk FB, Tuinzing DB. Complications in bilateral mandibular distraction osteogenesis using internal devices. *Oral Surgery, Oral Medicine, Oral Pathology, Oral Radiology, and Endodontics* 2003 Oct;96(4): 392–397. doi: 10.1016/s1079-2104(03)00472-4

[xiii] Von Bremen J, Schafer D, Kater W, Ruf S. Complications during mandibular midline distraction: the first 100 patients. *Angle Orthodontist* 2008;78:20–24.

[xiv] Ow A, Cheung LK. Skeletal stability and complications of bilateral sagittal split osteotomies and mandibular distraction osteogenesis: an evidence-based review. *Journal of Oral and Maxillofacial Surgery* 2009 Nov;67(11):2344–2353. doi: 10.1016/j.joms.2008.07.003

[xv] van Strijen PJ, Perdijk FB, Becking AG, Breuning KH. Distraction osteogenesis for mandibular advancement. *International Journal of Oral and Maxillofacial Surgery* 2000 Apr;29(2):81-5. doi: 10.1034/j.1399-0020.2000.290201.x

[xvi] Panjabi MM, Walter SD, Karuda M, White AA, Lawson JP. Correlations of radiographic analysis of healing fractures with strength: a statistical analysis of experimental osteotomies. *Journal of Orthopaedic Research* 1985;3(2):212–218. doi: 10.1002/jor.1100030211

[xvii] Hipp JA, Springfield DS, Hayes WC. Predicting pathologic fracture risk in the management of metastatic bone defects. *Clinical Orthopaedics and Related Research* 1995(312):120–135. PubMed PMID: 7634597.

[xviii] Simpson AH, Kenwright J. Fracture after distraction osteogenesis. *Journal of Bone and Joint Surgery. British Volume* 2000;82(5):659–665. doi: 10.1302/0301-620x.82b5.9945

[xix] Launay F, Younsi R, Pithioux M, Chabrand P, Bollini G, Jouve JL. Fracture following lower limb lengthening in children: a series of 58 patients. *Orthopaedics & Traumatology, Surgery & Research: OTSR* 2013;99(1):72–79. doi: 10.1016/j.otsr.2012.08.005

[xx] Kitoh H, Mishima K, Matsushita M, Nishida Y, Ishiguro N. Early and late fracture following extensive limb lengthening in patients with achondroplasia and hypochondroplasia. *Bone & Joint Journal* 2014;96-B(9):1269–1273. doi: 10.1302/0301-620X.96B9.33840

[xxi] Burke NG, Cassar-Gheiti AJ, Tan J, McHugh G, O'Neil BJ, Noonan M, Moore D. Regenerate bone fracture rate following femoral lengthening in paediatric patients. *Journal of Children's Orthopaedics* 2017;11(3):210–215. doi: 10.1302/1863-2548.11.160216

[xxii] Eldridge JC, Bell DF. Problems with substantial limb lengthening. *Orthopedic Clinics of North America* 1991;22(4):625–631. PubMed PMID: 1945340.

[xxiii] Danziger MB, Kumar A, DeWeese J. Fractures after femoral lengthening using the Ilizarov method. *Journal of Pediatric Orthopedics* 1995;15(2):220–223. PubMed PMID: 7745098.

[xxiv] Castelein S, Docquier PL. Complications associated with bone lengthening of the lower limb by callotasis. *Acta Orthopaedica Belgica* 2016;82(4):806–813. PubMed PMID: 29182122.

[xxv] Nazarian A, Entezari V, Zurakowski D, Calderon N, Hipp JA, Villa-Camacho JC, Lin PP, Cheung FH, Aboulafia AJ, Turcotte R, Anderson ME, Gebhardt MC, Cheng EY, Terek RM, Yaszemski M, Damron TA, Snyder BD. Treatment Planning and Fracture Prediction in Patients with Skeletal Metastasis with CT-Based Rigidity Analysis. *Clinical Cancer Research* 2015;21(11):2514–2519. doi: 10.1158/1078-0432.CCR-14-2668

[xxvi] Panjabi MM, Walter SD, Karuda M, White AA, Lawson JP. Correlations of radiographic analysis of healing fractures with strength: a statistical analysis of experimental osteotomies. *Journal of Orthopaedic Research* 1985;3(2):212–218. doi: 10.1002/jor.1100030211

[xxvii] Hipp JA, Springfield DS, Hayes WC. Predicting pathologic fracture risk in the management of metastatic bone defects. *Clinical Orthopaedics and Related Research* 1995(312):120–135. PubMed PMID: 7634597.

[xxviii] Babatunde OM, Fragomen AT, Rozbruch SR. Noninvasive quantitative assessment of bone healing after distraction osteogenesis. *HSS Journal* 2010;6(1):71–78. doi: 10.1007/s11420-009-9130-y

[xxix] Moed BR, Kim EC, van Holsbeeck M, Schaffler MB, Subramanian S, Bouffard JA, Craig JG. Ultrasound for the early diagnosis of tibial fracture healing after static interlocked nailing without reaming: histologic correlation using a canine model. *Journal of Orthopaedic Trauma* 1998;12(3):200–205. doi: 10.1097/00005131-199803000-00012

[xxx] Bail HJ, Kolbeck S, Krummrey G, Weiler A, Windhagen HJ, Hennies K, Raun K, Raschke MJ. Ultrasound can predict regenerate stiffness in distraction osteogenesis.

Clinical Orthopaedics and Related Research 2002(404):362–367. doi: 10.1097/00003086-200211000-00053

[xxxi] Rosenfeld, A. and Kak, A.C. (1982) *Digital Picture Processing*. 2nd Edition, Academic Press, New York.

[xxxii] S. Minaee, Y. Boykov, F. Porikli, A. Plaza, N. Kehtarnavaz and D. Terzopoulos, Image Segmentation Using Deep Learning: A Survey. *IEEE Transactions on Pattern Analysis and Machine Intelligence* 2022 July;44(7):3523–3542. doi: 10.1109/TPAMI.2021.3059968.

[xxxiii] Segmenting unwanted regions from the image has been a fundamental problem in computer vision since early days of the field.

[xxxiv] Nameirakpam Dhanachandra, Khumanthem Manglem, Yambem Jina Chanu, Image Segmentation Using K -means Clustering Algorithm and Subtractive Clustering Algorithm, *Procedia Computer Science* 2015;54:764–771. https://doi.org/10.1016/j.procs.2015.06.090

[xxxv] Nameirakpam Dhanachandra, Khumanthem Manglem, Yambem Jina Chanu, Image Segmentation Using K -means Clustering Algorithm and Subtractive Clustering Algorithm, *Procedia Computer Science* 2015;54:764–771. https://doi.org/10.1016/j.procs.2015.06.090

[xxxvi] Kass, M., Witkin, A. & Terzopoulos, D. Snakes: Active contour models. *International Journal of Computer Vision* 1988;1:321–331. https://doi.org/10.1007/BF00133570

[xxxvii] zephyr (2023). Automatic Thresholding (https://www.mathworks.com/matlabcentral/fileexchange/3195-automatic-thresholding), MATLAB Central File Exchange. Retrieved October 25, 2023.

[xxxviii] J. S. Weszka, R. N. Nagel and A. Rosenfeld. A Threshold Selection Technique. *IEEE Transactions on Computers* 1974 Dec;C-23(12):1322–1326. doi: 10.1109/T-C.1974.223858

[xxxix] Linda G. Shapiro and George C. Stockman (2001), *Computer Vision*, pp 279–325, New Jersey, Prentice-Hall, ISBN 0-13-030796-3

[xl] Barghout, Lauren, and Lawrence W. Lee. “Perceptual information processing system." Paravue Inc. U.S. Patent Application 10/618,543 filed July 11, 2003.

[xli] Simpson AH, Kenwright J. Fracture after distraction osteogenesis. *Journal of Bone and Joint Surgery. British Volume* 2000;82:659–665.

xlii Zarzycki D, Tesiorowski M, Zarzycka M, Kacki W, Jasiewicz B. Long-term results of lower limb lengthening by the Wagner method. *Journal of Pediatric Orthopedics* 2002;22:371–374.

xliii Antoci V, Ono CM, Antoci Jr V, Raney EM. Bone lengthening in children: how to predict the complications rate and complexity? *Journal of Pediatric Orthopedics* 2006;26:634–640.

xliv Launay F, Younsi R, Pithioux M, Chabrand P, Bollini G, Jouve JL. Fracture following lower limb lengthening in children: a series of 58 patients. *Orthopaedics & Traumatology, Surgery & Research: OTSR* 2013 Feb;99(1):72–79. doi: 10.1016/j.otsr.2012.08.005

xlv Saran N, Hamdy RC. DEXA as a predictor of fixator removal in distraction osteogenesis. *Clinical Orthopaedics and Related Research* 2008;466:2955–2961.

xlvi Tselentakis G, Owen PJ, Richardson JB, Kuiper JH, Haddaway MJ, Dwyer JS, et al. Fractures stiffness in callotasis deter- mined by Dual-Energy X-Ray Absorptiometry scanning. *Journal of Pediatric Orthopedics. Part B* 2001;10:248–254.

xlvii Young JWR, Kostrubiak IS, Resnick CS, Paley D. Sonographic evaluation of bone production at the distraction site in limb lengthening procedures. *American Journal of Roentgenology* 1990;154:125–128.

xlviii Chotel F, Braillon P, Gadeyne S. Bone stiffness in children. Part I. *In vivo* assessment of the stiffness of femur and tibia in children. *Journal of Pediatric Orthopedics* 2008;28:534–537.

xlix Zhao L, Fan Q, Venkatesh KP, Park MS, Song HR. Objective guidelines for removing an external fixator after tibial length- ening using pixel value ratio. A pilot study. *Clinical Orthopaedics and Related Research* 2009;467:3321–3326.

l Romanowski CA, Underwood AC, Sprigg A. Reduction of radi- ation doses in leg lengthening procedures by means of audit and computed tomography scanogram techniques. *British Journal of Radiology* 1994;67:1103–1107.

li Eyres KS, Bell MJ, Kanis JA. Methods of assessing new bone for- mation during limb lengthening. Ultrasonography, dual energy X-ray absorptiometry and radiography compared. *Journal of Bone and Joint Surgery. British Volume* 1993; 75:358–364.

lii Gilbert SF. *Developmental Biology*. 6th edition. Sunderland (MA): Sinauer Associates; 2000. Osteogenesis: The Development of Bones. Available from: https://www.ncbi.nlm.nih.gov/books/NBK10056/#

[liii] Adele Boskey. Bone mineral crystal size. *Osteoporosis International* 2003;14 (Suppl 5):16–21. https://doi.org/10.1007/s00198-003-1468-2

[liv] Mettler FA, Guiberteau MJ. *Essentials of Nuclear Medicine Imaging*. 6th ed. Philadelphia, PA: Elsevier Saunders; 2012, Chapter 8: 305–309.

[lv] Doroudinia, Abtin; Colletti, Patrick M. Bone Mineral Measurements. *Clinical Nuclear Medicine* 2015 Aug;40(8):647–657. DOI: 10.1097/RLU.0000000000000860

[lvi] Genant HK, Engelke K, Fuerst T, Glüer CC, Grampp S, Harris ST, Jergas M, Lang T, Lu Y, Majumdar S, Mathur A, Takada M. Noninvasive assessment of bone mineral and structure: state of the art. *Journal of Bone and Mineral Research* 1996 Jun;11(6):707–730. doi: 10.1002/jbmr.5650110602

[lvii] Wahner HW, Dunn WL, Brown ML, Morin RL, Riggs BL. Comparison of dual-energy x-ray absorptiometry and dual photon absorptiometry for bone mineral measurements of the lumbar spine. *Mayo Clinic Proceedings* 1988 Nov;63(11): 1075–1084. doi: 10.1016/s0025-6196(12)65502-5

[lviii] Cullum ID, Ell PJ, Ryder JP. X-ray dual-photon absorptiometry: a new method for the measurement of bone density. *British Journal of Radiology* 1989 Jul;62(739): 587–592. doi: 10.1259/0007-1285-62-739-587

[lix] Mazess R, Collick B, Trempe J, Barden H, Hanson J. Performance evaluation of a dual-energy x-ray bone densitometer. *Calcified Tissue International* 1989 Mar; 44(3):228–232. doi: 10.1007/BF02556569

[lx] Glen M. Blake, Ignac Fogelman. Technical principles of dual energy X-ray absorptiometry. *Seminars in Nuclear Medicine* 1997;27(3):210–228.

[lxi] Svendsen OL, Hassager C, Skødt V, Christiansen C. Impact of soft tissue on in vivo accuracy of bone mineral measurements in the spine, hip, and forearm: a human cadaver study. *Journal of Bone and Miner Research* 1995 Jun;10(6):868–873. doi: 10.1002/jbmr.5650100607

[lxii] Keklikoglou K, Arvanitidis C, Chatzigeorgiou G, Chatzinikolaou E, Karagiannidis E, Koletsa T, Magoulas A, Makris K, Mavrothalassitis G, Papanagnou ED, Papazoglou AS, Pavloudi C, Trougakos IP, Vasileiadou K, Vogiatzi A. Micro-CT for Biological and Biomedical Studies: A Comparison of Imaging Techniques. *Journal of Imaging* 2021 Sep 1;7(9):172. doi: 10.3390/jimaging7090172

[lxiii] Kim Y, Brodt MD, Tang SY, Silva MJ. MicroCT for Scanning and Analysis of Mouse Bones. *Methods in Molecular Biology* 2021;2230:169–198. doi: 10.1007/978-1-0716-1028-2_11

[lxiv] Bryda EC. The Mighty Mouse: the impact of rodents on advances in biomedical research. *Missouri Medicine* 2013 May–Jun;110(3):207–211. PMID: 23829104; PMCID: PMC3987984.

[lxv] Bruder S, Fox B. Tissue engineering of bone. Cell based strategies. *Clinical Orthopaedics and Related Research* 1999;367 (suppl.):S68–83.

[lxvi] Cancedda R, Dozin B, Giannoni P, Quarto R. Tissue engineering and cell therapy of cartilage and bone. *Matrix Biology* 2003;22:81–91.

[lxvii] Reddi A. Morphogenesis and tissue engineering of bone and cartilage: inductive signals, stem cells, and biomimetic biomaterials. *Tissue Engineering* 2000;6:351–359

[lxviii] Trinavarat P.,Kritsaneepaiboon S.,Rongviriyapanich C.,Visrutaratna P. and Srinakarin J. Radiation dose from CT scanning: can it be reduced? *Asian Biomedicine* 2017;5(1):13–21. https://doi.org/10.5372/1905-7415.0501.002

[lxix] Zuoyong Li, Chuancai Liu, Guanghai Liu, Yong Cheng, Xibei Yang, Cairong Zhao, A novel statistical image thresholding method, *AEU - International Journal of Electronics and Communications* 2010;64(12):1137–1147. https://doi.org/10.1016/j.aeue.2009.11.011

[lxx] N. Otsu, A Threshold Selection Method from Gray-Level Histograms. *IEEE Transactions on Systems, Man, and Cybernetics* 1979 Jan;9(1):62–66. doi: 10.1109/TSMC.1979.4310076.

[lxxi] Yi Wan, Jiangchang Wang, Xingbo Sun and Ming Ha. A modified Otsu image segment method based on the Rayleigh distribution. *2010 3rd International Conference on Computer Science and Information Technology*, Chengdu, China, 2010, pp. 281–285, doi: 10.1109/ICCSIT.2010.5563957

[lxxii] E. Meijering. A chronology of interpolation: from ancient astronomy to modern signal and image processing. *Proceedings of the IEEE* 2002 March;90(3):319–342. doi: 10.1109/5.993400

[lxxiii] Hipp JA, Springfield DS, Hayes WC. Predicting pathologic fracture risk in the management of metastatic bone defects. *Clinical Orthopaedics and Related Research* 1995;312:120–135.

[lxxiv] WhealanKM, KwakSD, Tedrow JR, Inoue K, Snyder BD. Noninvasive imaging predicts failure load of the spine with simulated osteolytic defects. *Journal of Bone and Joint Surgery. American Volume* 2000;82:1240–1251.

[lxxv] Cory E, Nazarian A, Entezari V, Vartanians V, Müller R, Snyder BD. Compressive axial mechanical properties of rat bone as functions of bone volume fraction, apparent density and micro-ct based mineral density. *Journal of Biomechanics* 2010 Mar 22;43(5):953–960. doi: 10.1016/j.jbiomech.2009.10.047

[lxxvi] Brody-Camp S, Winters R. Craniofacial Distraction Osteogenesis. [Updated 2023 Jul 24]. In: StatPearls [Internet]. Treasure Island (FL): StatPearls Publishing; 2024 Jan-. Available from: https://www.ncbi.nlm.nih.gov/books/NBK560915/

CURRICULUM VITAE

[redacted]

[redacted]

[redacted]